Surface Tension and Electroporation of Lipid Bilayers

by

Han-Jae Jeremy Cho

B.S.E., Mechanical Engineering (2009)

University of Michigan

Submitted to the Department of Mechanical Engineering in

Partial Fulfillment of the Requirements for the

Degree of Master of Science in Mechanical Engineering

at the

Massachusetts Institute of Technology

June 2011

Signature of Author: .....

Department of Mechanical Engineering

May 6, 2011

Certified by: .....

Evelyn N. Wang

Assistant Professor of Mechanical Engineering

Thesis Supervisor

Accepted by: .....

David E. Hardt

Chairman, Department Committee on Graduate Theses

Surface Tension and Electroporation of Lipid Bilayers

by

Han-Jae Jeremy Cho

Submitted to the Department of Mechanical Engineering on May 6th, 2011,
in Partial Fulfillment of the Requirements for the Degree of Master of Science

Abstract

Electroporation of lipid bilayers is widely used in DNA transfection, gene therapy, and targeted drug delivery and has potential applications in water desalination and filtration. A better, more thorough molecular understanding is needed, however, before such devices can be effectively used and developed. From aqueous pore formation theory, electroporation behavior is known to be largely dictated by surface energy. We hypothesize that this surface energy can be described by separate head and tail components of the lipid molecules, which can be obtained experimentally. In this thesis, we demonstrated a basic ability to electroporate lipid bilayers as well as verify its electrical behavior. We formed lipid monolayer and bilayer films and studied their wetting properties using water, formamide, and diiodomethane. We determined that the strong interaction between polar liquids (water and formamide) and hydrophilic substrates (mica and glass) can affect the wetting behavior and quality of films. In addition, we verified that the resulting surface energy of lipid tails is mostly nonpolar. The insights of this work offer a first step towards characterizing the surface energies of different lipids and how they relate to the electroporation behavior.

Thesis Supervisor: Evelyn N. Wang
Title: Assistant Professor, Mechanical Engineering

Acknowledgements

I would like to thank my advisor, Professor Evelyn Wang, for her encouraging support and guidance over the past two years. She has always helped me understand what I needed to do especially when the goal of my research isn't always completely defined. I would also like to thank members in the Device Research Laboratory for feedback and support. In particular, Dr. Shalabh Maroo, Dr. Ryan Enright, Tom Humplik, and Batya Fellman were extremely helpful in our subgroup meetings and discussions. I would also like to thank Jenny Qiu for her help in designing and building a new experimental setup. I also owe a debt gratitude to my friends and family who, despite not completely understanding what I do, have consistently encouraged me to pursue this career of mine in research and have kept me grounded all these years.

This research would not have been possible without the use of facilities from the Institute of Soldier Nanotechnologies, Microsystems Technology Laboratories, and Professor Timothy Swager's laboratory. In addition, I also thank Professor Marco Colombini of the University of Maryland who helped me with membrane formation methods. Finally, this work was supported in part by the MRSEC Program of the National Science Foundation under award number DMR - 0819762.

Contents

List of Figures

Chapter 1: Introduction

Motivation

Lipid bilayers constitute cell membranes and can form nanopores when an electric field is applied in a phenomenon called electroporation. These pores increase the permeability of the bilayer. Since the early 1990s, electroporation has been used for DNA and gene transfection. Recently, the phenomenon has been utilized for targeted cell drug delivery, such as in electrochemotherapy [1]. To perform electroporation on cells, however, much of the parameters such as electric pulse voltage and frequency must be determined in an *ad hoc* fashion and the applicability is limited to only a few cell types. Thus, a more thorough and fundamental understanding of the electroporation phenomenon could improve the efficacy of cell based electroporation applications in medicine and molecular biology.

Electroporation can also have potential use for desalination. Due to growing demands for scarce fresh water supplies, improving water desalination methods has become increasingly important. Desalination is attractive since it provides access to the virtually limitless supply of seawater. However, rapid adoption of this technology is hampered by the high capital costs and energy usage required to build and operate these facilities [2]. Reverse osmosis (RO), which is currently the least energetically demanding technology, filters salt ions by the forcing fluid through a semi-permeable membrane. The high pressure required is a primary reason for large energy cost requirements for desalination. Commercial RO membranes accomplish water transport by diffusion, which typically offer hydraulic permeabilities of around 10^{-12} m/Pa·s. If pore size in an electroporating lipid bilayer can be controlled to sub nanometer length scales, then solvated salt ions can be rejected by size based exclusion as shown in Figure 1 and the membrane could potentially offer permeabilities on the order of 10^{-11} m/Pa·s [3]. Since the energy required to flow liquid through a porous media is inversely proportional to the permeability, electroporating lipid bilayers could possibly offer order of magnitude range decreases in energy consumption.

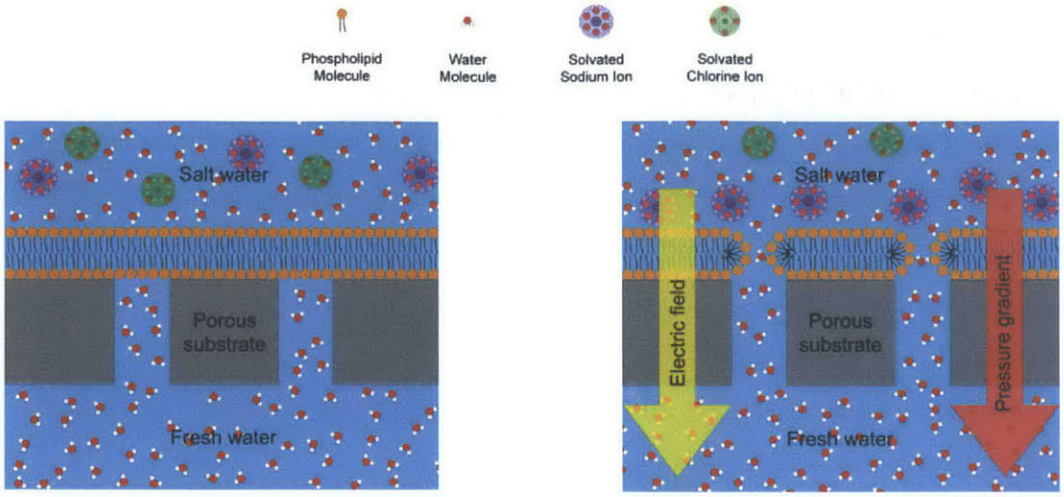

Figure 1: Proposed concept where a lipid bilayer membrane is supported on a nanoporous substrate for water desalination. Lipid bilayer membrane behavior **(a)** under no electric field and **(b)** when an electric field and pressure ($P > P_{osmotic}$) are applied. When electroporated, the controlled pores allow only water to pass through the permeabilized membrane.

Another high cost associated with desalination plants is anti-fouling measures. There are some potential benefits in using lipids in regard to this area as well. The zwitterionic, hydrophilic heads on phospholipids are naturally resistant to certain types of proteins [4] and has been shown to improve overall fouling resistance [5, 6]. The fact that lipid bilayers could be reconstructed easily via vesicle fusion is also a benefit. If a lipid bilayer membrane were to be damaged by excessive fouling, it could easily be dissolved and reformed through immersion in a lipid vesicle solution, providing a relatively quick and low-cost solution to remake membranes.

The electroporating lipid bilayer also has attractive capabilities that could be useful in other engineering applications. Such a membrane could be actively controlled such as an "on or off" switch, and the effective pore size could be varied. As a gate, flow can be regulated and/or filtering can be activated according to desired timing. As a variable sized filter, the size criteria for accepting or rejecting a particle could be actively varied. Such behavior could be useful for pulsatile drug delivery [7] and regulation of flow in microfluidic systems.

Background

Phospholipids

Lipids are a broad group of naturally occurring molecules, which perform important biological functions such as energy storage, structural components of cell membranes, and signaling molecules. Phospholipids are a class of lipids macroscopically characterized by having a hydrophilic head and two hydrophobic tails (Figure 2a). The head is a zwitterionic compound such as phosphocholine while the tail is composed of two fatty acids. The head and tails are joined together by a glycerol backbone. Phosphocholine is often seen as the head of the lipid while different fatty acids of varying carbon chain lengths with saturated and unsaturated configurations can be seen as the tails.

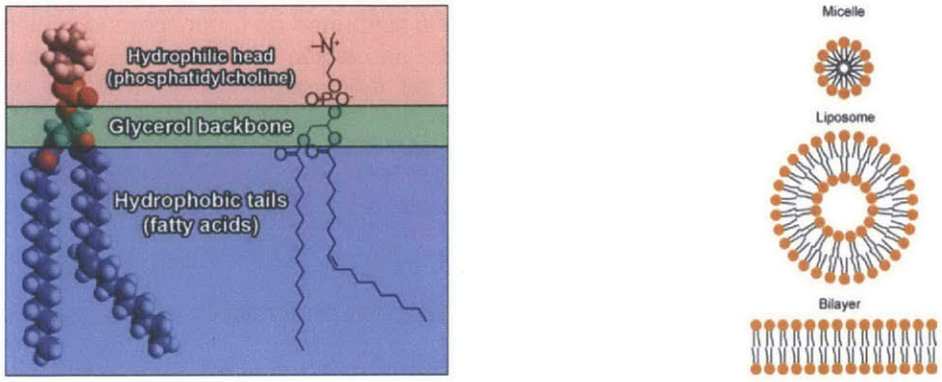

Figure 2: (a) Structure of a phospholipid with two fatty acids palmitoyl (saturated) and oleoyl (unsaturated). The kink the oleoyl fatty acid is due the cis isomerism of a double bond in the carbon chain. **(b)** Different aggregate structures of phospholipids.

When immersed in water, phospholipids orient themselves such that hydrophilic heads are in contact with water, thus forming a lipid bilayer (Figure 2b). In the opposite case of an apolar liquid, the tails orient themselves outward and heads inward. Due to the hydrophobic interior, these bilayers are mostly impervious to water and ions; however, when subject to an electric field, nanometer sized pores form in the lipid bilayer membrane which results in an increased permeability across the membrane, and provides access to the cytoplasm if the membrane encompasses a biological cell. If the bilayer is not supported or suspended about a hole, the bilayer will collapse into a liposome/vesicle or micelle.

In the biological cell membrane, lipid bilayers serve as the underlying template onto which proteins, cholesterol, and other lipids are added. Much of the semi-permeable behavior attributed to cell membranes is due to the numerous channels and ion pumps embedded within the membrane. For instance, aquaporins and ion channels selectively pass water and ions across the membrane, respectively, via diffusion. Ion pumps, on the other hand, force ions across the membrane against the concentration gradient.

Two lipids are used in this study: diphytanoylphosphatidylcholine (DiPhyPC) and dipalmitoylphosphatidylcholine (DPPC) (see Figure 3). The former was used for electroporation while the latter for wetting experiments. DiPhyPC is a phytanic analog of DPPC; they have the same tail length and headgroup but DiPhyPC has additional CH_3 groups attached to the chain. Physically, DiPhyPC has a much lower gel-fluid transition temperature (< -120°C [8]) compared to that of DPPC (41°C). Therefore, at room temperature, DiPhyPC is in a fluid state whereas DPPC is in a gel-crystalline state.

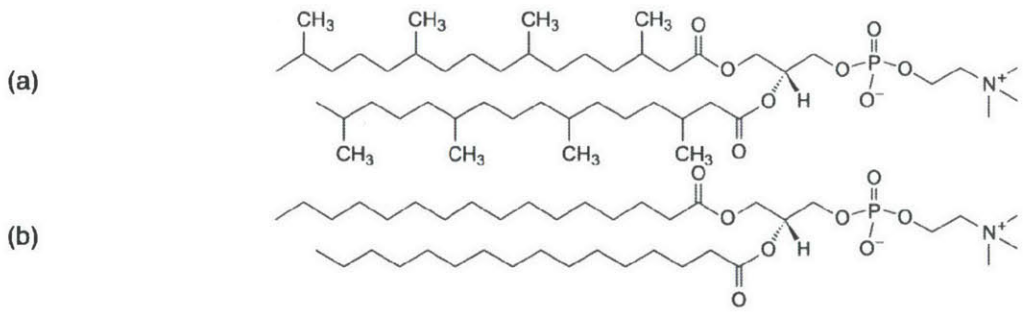

Figure 3: (a) DiPhyPC which is used for electroporation studies and **(b)** DPPC used for wetting studies.

Theory of Electroporation

Electroporation is the enhanced permeability of a lipid bilayer when an external electric field is applied. The phenomenon was originally observed in cells and artificial lipid bilayers in the 1970s [9, 10] and over the 1980s and 1990s aqueous pore formation theory, the most accepted theoretical view of electroporation, was developed.

The theory is based on thermodynamics that states the energy required to form a hole in a two-dimensional film is equal to the work required to create the hole edge minus the surface energy lost due to decrease in surface area. This is expressed as

$$W(r) = 2\pi r\Gamma - \pi r^2 \gamma_{\text{bilayer}} \qquad \textbf{Equation 1}$$

where Γ is the edge tension, γ_{bilayer} is the surface tension, and r is the radius of the hole. The edge energy term is positive since energy is required to create an edge and the surface energy term is negative since energy is lost from a reduction in surface area. Hence, surface and edge energies play an important role in the behavior of electroporation. In the simple case where Γ and γ_{bilayer} are constant, this free energy curve is parabolic; thus, once a pore exceeds a critical radius of $\Gamma/\gamma_{\text{bilayer}}$, the pore will expand until rupture. As shown in Figure 4, below the critical radius, the pore will contract back to its initial state.

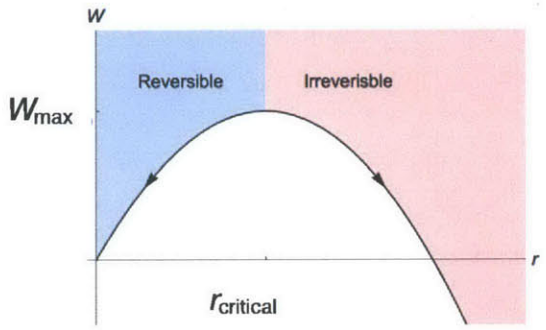

Figure 4: Simple parabolic model of thermodynamic pore formation of constant edge and surface tension. When $r < r_{critical}$, the pore is reversible. Beyond $r_{critical}$, the pore expands until rupture.

However, this simple model is not an accurate representation of electroporation. 1) The effect of voltage on the energy of a pore is not captured. 2) As a pore grows larger, the strong polar interactions between heads will cause lipids to reorient themselves such that the inner pore wall is lined with heads; thus, a hydrophilic pore is favorable at larger pore radii. At small pore radii, a hydrophobic pore is favorable due to the steric interactions between heads. Thus, we can define the total energy to create a pore as [11]

$$W(r,U) = \left(\begin{cases} \dfrac{2\pi r d \gamma_h I_1\left(\frac{r}{\lambda}\right)}{I_0\left(\frac{r}{\lambda}\right)} - \pi r^2 \gamma_{\text{bilayer}} - \dfrac{\left((\varepsilon_e - \varepsilon_m)\pi r^2\right) U^2}{2d} & r < r_p \\ \left(\dfrac{C}{r}\right)^4 + 2\pi r\Gamma - \pi r^2 \gamma_{\text{bilayer}} - \dfrac{\left((\varepsilon_e - \varepsilon_m)\pi r^2\right) U^2}{2d} & r > r_p \end{cases} \right) \qquad \textbf{Equation 2}$$

where the pore is hydrophobic when $r < r_p$ and hydrophilic when $r > r_p$. In both hydrophobic and hydrophilic regimes, the energy is decreased by an electric capacitance term that is dependent on the dielectric permittivities of the aqueous medium ε_e and bilayer ε_e, the bilayer thickness d and the electric potential U. According to Glaser *et al.* [12], the hydrophobic edge tension can be defined in terms of the bilayer thickness d, a hydrophobic surface tension γ_h, and a characteristic length of interaction λ, where r is varied by the modified Bessel functions of the first kind I_n. The result is a steep rise in the energy as pore size grows. In the hydrophilic case, the steric interaction term $(C/r)^4$ causes a steep rise in energy when the heads become too close. The combined effect of voltage on the energy of a pore as well as the molecular reorientation is shown in Figure 5.

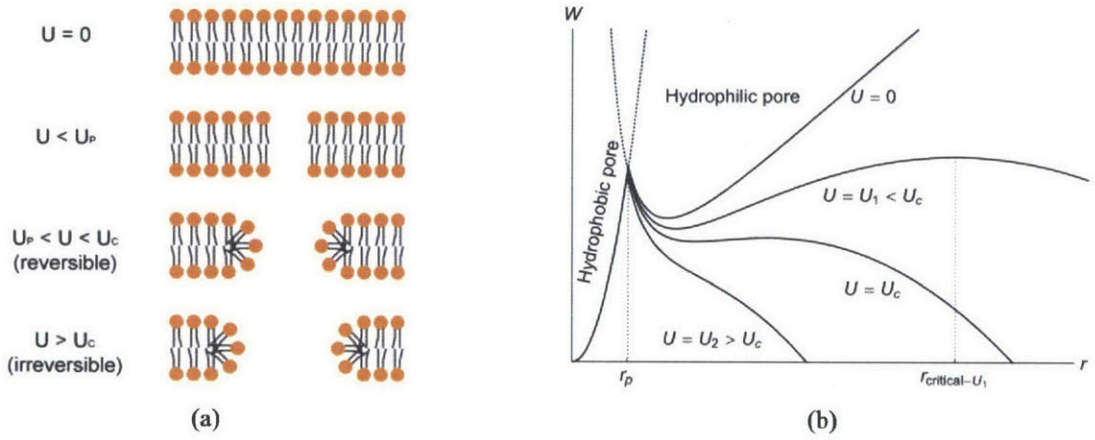

Figure 5: (a) Schematic showing electroporation of a lipid bilayer where U is the applied voltage, U_P is the voltage for the onset of poration, and U_C is the critical irreversible breakdown voltage. (b) The work to create a pore, W, based on the aqueous pore formation model with voltage dependencies where $U_2 > U_1 > 0$. When $r < r_p$, the pore is hydrophobic and when $r > r_p$, the pore transitions to hydrophilic by a rearrangement of the heads. The voltage affects the stability of the hydrophilic pore. At $U = U_1 < U_c$, the hydrophilic pore can reseal upon removal of applied voltage leading to reversible electroporation as long as the radius of the pore $r < r_{critical\text{-}U1}$. At $U = U_2 > U_c$, the hydrophilic pore is unstable and will expand until rupture causing irreversible electroporation.

According to this model, the initial activation energy required to transition from a hydrophobic to a hydrophilic pore at r_p is weakly dependent on the voltage. However, the stability of the pore is highly dependent on voltage as shown in Figure 5b. When no electric potential is applied, a small distribution of metastable pores may exist with a certain Boltzmann probability

$$P(W_{\text{metastable}}) = \frac{e^{-\frac{W_{\text{metastable}}}{k_B T}}}{Q} \qquad \textbf{Equation 3}$$

where Q is the partition function and $W_{\text{metstable}}$ is the energy of a metastable pore which is the local minimum of the pore energy when $r > r_p$. When a potential is applied, the energy of the hydrophilic pore decreases causing the metastable pore to become unstable and expand until the bilayer is ruptured as shown by the $U = U_2 > U_c$ curve in Figure 5b. Here, U_c is critical or breakdown voltage. This behavior effectively describes *irreversible* electroporation. In the case of reversible electroporation, the metastable pore is made unstable as before and grows. However, before rupture occurs, the potential is quickly removed, effectively shifting the energy profile to the $U = 0$ curve in Figure 5b. As long as the pore radius is smaller than that of the maximum energy of the pore at $U = 0$, the pore will return to its closed or metastable state. This rapid addition and removal of an electric potential (a voltage pulse) results in *reversible* electroporation. The time averaged pore size and hence the recovery time should be highly dependent on the pulse time which has been shown experimentally by Chernomordik *et al.* [13].

As shown by Equation 2, the energy required to electroporate a membrane is highly dependent on the surface and edge energies of the pore. If a highly tunable electroporation membrane is desired, then the surface and edge energies should allow a wide window in time in which to apply an electric pulse such that the average pore size can be effectively controlled. By revisiting the simple parabolic model in Figure 4, increasing r_{critical} will allow for a larger range of reversibility, *i.e.*, the edge energy, Γ, should be large compared to the surface tension, γ_{bilayer}.

Surface and edge energies

To determine an ideal electroporation membrane based on surface and edge energy properties, an understanding of how chemical parameters affect these properties is necessary. Furthermore, despite significant research in electroporation [11, 14-17], quantifying molecular phenomena experimentally is difficult. Thus, to simplify our approach to examining surface and energy terms, we seek to describe these properties as separate contributions from the heads and tails. As a first step, we can describe the edge tension as a surface energy where $\Gamma = d\gamma_{\text{edge}}$. The γ_{edge} term is essentially the surface tension of the inner wall of the pore as illustrated in Figure 6a. The benefit of treating the membrane as a three-dimensional slab as opposed to a two-

dimensional sheet is that the edge energy can be expressed in terms of an experimentally measurable surface tension. The basic form of Equation 1 becomes

$$W(r, U) = 2\pi r d \gamma_{\text{edge}} - \gamma_{\text{bilayer}} \pi r^2 - \frac{\left((\varepsilon_e - \varepsilon_m)\pi r^2\right) U^2}{2d} \qquad \textbf{Equation 4}$$

where the overall behavior is lumped into a single equation and γ_{edge} is dependent on r. Furthermore, we assume the heads and tails have their own independent surface tensions γ_{head} and γ_{tail}, where each term represents the average force interaction between heads or tails within a film in the absence of the other as shown in Figure 6b.

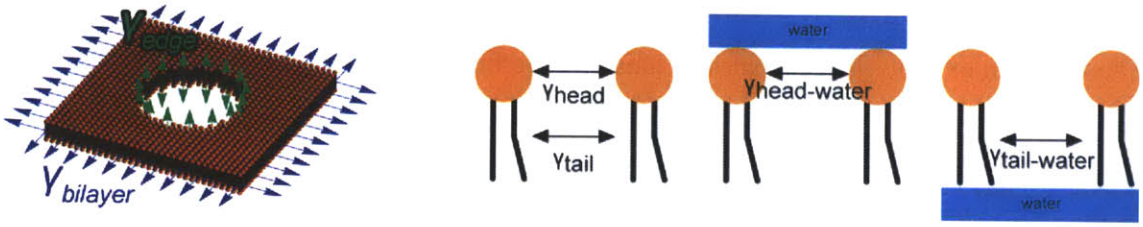

(a) (b)

Figure 6: (a) Schematic of the bilayer and hole edge surface tensions which are modeled as **(b)** independent interactions of the lipid heads, tails, and water

With this treatment of the surface energies, we can begin to describe γ_{edge} and γ_{bilayer} in terms of γ_{head} and γ_{tail}. Since the inner wall is composed of heads and tails, the edge surface energy should be a function of the independent interfacial head and tail surface tensions.

$$\gamma_{\text{edge}} = f\left(\gamma_{\text{head,water}}, \gamma_{\text{tail,water}}\right) \qquad \textbf{Equation 5}$$

We can relate the different interfacial surface tensions together by the Young equation where our solid in this case is either the heads or the tails and θ is the contact angle of a probe liquid on a solid surface.

$$\gamma_{\text{solid,vapor}} = \gamma_{\text{solid,liquid}} + \gamma_{\text{liquid,vapor}} \cos(\theta) \qquad \textbf{Equation 6}$$

The interfacial surface tensions can also be defined in terms of the surface energy by the Young-Dupre equation where $W_{1,2}$ is the work of adhesion between two phases.

$$W_{1,2} = \gamma_1 + \gamma_2 - \gamma_{1,2} \qquad \textbf{Equation 7}$$

When one of the phases is air at standard conditions, $W_{i,air}$ and γ_{air} is usually negligible. Hence, $\gamma_{i,air} \approx \gamma_{air}$. By combining Equation 6 and Equation 7 with this approximation, the solid-liquid interfacial tension as a function of the liquid surface tension (usually known) and the contact angle can be determined.

$$\gamma_{solid,liquid} = \gamma_{solid} - \gamma_{liquid}\cos(\theta) \qquad \textbf{Equation 8}$$

Thus, we can express the edge surface tension in terms of experimentally determinable parameters.

$$\gamma_{edge} = f\left(\gamma_{head}, \gamma_{tail}, \theta_{head,water}, \theta_{tail,water}\right) \qquad \textbf{Equation 9}$$

The surface tension of the bilayer on the other hand should be mostly dependent on the heads since no tails are in contact with water on the top and bottom surfaces of the lipid bilayer. Using a similar approximation as before, we can express the surface tension of the bilayer.

$$\gamma_{bilayer} \simeq 2\,\gamma_{head,water} = 2\left(\gamma_{head} - \gamma_{water}\cos\left(\theta_{head,water}\right)\right) \qquad \textbf{Equation 10}$$

The factor of two is due to the fact that there are two head-water interfaces on the lipid bilayer (top and bottom).

To determine the surface energy experimentally, we can use the Lifshitz-van der Waals acid-base (LWAB) approach [18, 19]. According to this theory, the total surface energy is a combination of Lifshitz-van der Waals interaction and a Lewis acid-base interaction.

$$\gamma_i = \gamma_i^{LW} + \gamma_i^{AB} \qquad \textbf{Equation 11}$$

where the acid-base interaction can be expressed in terms of an electron donor, γ^-, and an electron acceptor, γ^+, component.

$$\gamma_i^{AB} = 2\sqrt{\gamma_i^- \gamma_i^+} \qquad \textbf{Equation 12}$$

Using Equation 6, Equation 7, and the approximation to neglect effects of air, the work of adhesion between solid and liquid can be expressed in terms of the individual LWAB components.

$$W_{solid,liquid} = \gamma_{liquid}(1+\cos(\theta)) = 2\sqrt{\gamma_{solid}^{LW}\gamma_{liquid}^{LW}} + 2\sqrt{\gamma_{solid}^{+}\gamma_{liquid}^{-}} + 2\sqrt{\gamma_{solid}^{-}\gamma_{liquid}^{+}} \qquad \textbf{Equation 13}$$

Between three probe liquids of known γ^{LW}, γ^+, and γ^-, three different sessile drop wetting experiments can be performed where three different contact angles can be measured. By using Equation 13 for each case, a system of three equations can be used to solve three unknown surface energy components γ^{LW}, γ^+, and γ^-. By using Equation 11 and Equation 12, one can determine the total surface energy.

Thesis Objective and Outline

Attaining tunable electroporation lipid bilayer membranes for filtering and gating applications requires a comprehensive understanding of the fundamental molecular mechanics of the electroporation phenomenon. While much work has been done in the past, a comprehensive understanding of how different lipids have different electroporation behavior is lacking. It has been shown that the electroporation is highly dependent on the surface energies of the lipid. This thesis will detail the steps toward characterization of these surface energies and how wetting phenomena can be highly dictated by interactions between liquids and substrates.

In Chapter 2, we describe the formation of hydrated lipid membranes and preliminary tests to demonstrate electroporation behavior and characterize the electrical behavior.

In Chapter 3, we discuss formation, coating quality, and initial wetting tests of supported lipid films.

In Chapter 4, we show a detailed study of lipid films on mica using three different probe liquids.

In Chapter 5, we provide an analysis of the results of the mica study and corroborate wetting experiments with associated molecular dynamics results.

In Chapter 6, we summarize and conclude this work and discuss future directions.

Chapter 2: Formation of Hydrated Lipid Bilayers and their Electrical Behavior

Lipid Bilayer Formation Procedures

There are several methods to form a fully hydrated lipid bilayer in order to conduct electroporation experiments. The bilayer must be in contact with a polar solvent such as water from both sides. The painting method, which is the first method developed in 1962 [20] involves using a glass brush to "paint" a lipid dissolved in organic solvent across a small aperture on a hydrophobic partition which is immersed in an aqueous solution. While this method is fairly simple, a small amount of organic solvent is often trapped between the two molecular layers. The tip-dip technique [21] involves immersing a patch pipette into a solution with a lipid monolayer at the interface. During this immersion step, the pipette is under positive pressure. As it is pulled out of the solution, however, this pressure is released and a lipid film forms at the tip of the pipette as shown in Figure 7. The orientation of the lipids at the air-water interface is always such that heads are in contact with water while tails are exposed to air. The pipette is reintroduced to the surface again such that a bilayer forms by tail to tail contact. This method has the benefit of having small lipid bilayers where typical diameters are on the order of microns as well as having completely solvent free bilayers.

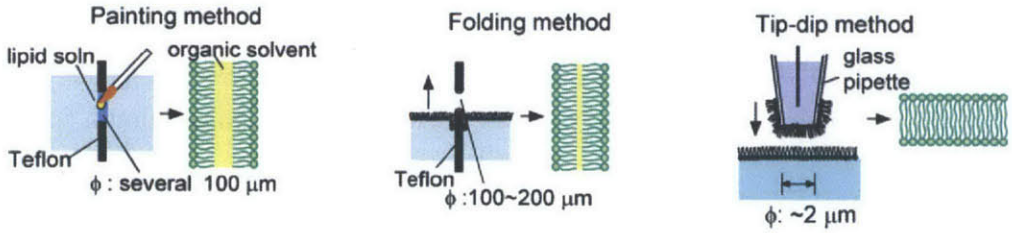

Figure 7: Three common ways to form hydrated lipid bilayers, the painting, folding and tip-dip method [22].

The method chosen for this study was the monolayer folding method as described by Montal and Mueller [23] and Colombini [24]. This method uses a similar setup as that of the painting method in that a hydrophobic partition with a small aperture is used. This aperture is coated with a solution of petroleum jelly in petroleum ether (5% w/v) such that an inner torus is

formed along the inside wall of the aperture. Lipids are then deposited on both sides of the partitions to form a lipid monolayer at the air-water interface. The level of liquid is slowly brought up over the hole allowing the two monolayers to fold together to form a lipid bilayer. Like the tip-dip method, the folding method produces a solvent free lipid but is much larger (typically ~100 μm in diameter). Once folding is completed, a lipid bilayer can be obtained as shown in Figure 8.

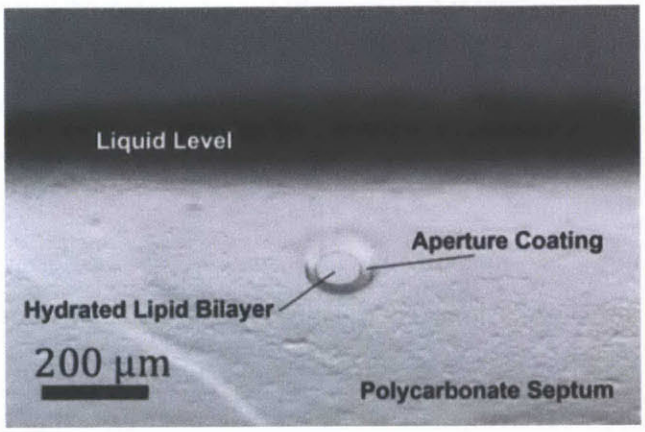

Figure 8: Formed fully hydrated DiPhyPC bilayer by monolayer folding method.

Experimental setup

A chamber setup was designed and built for lipid formation by the monolayer folding technique. The setup consists of a Teflon chamber separated into two halves by a partition. The partition is compressed between two rubber gaskets. Fluid connections allow the level of each chamber to be individually controlled by a syringe pump. Electrode ports allow access to Ag/AgCl electrodes to both chambers. All parts are secured within in an aluminum frame.

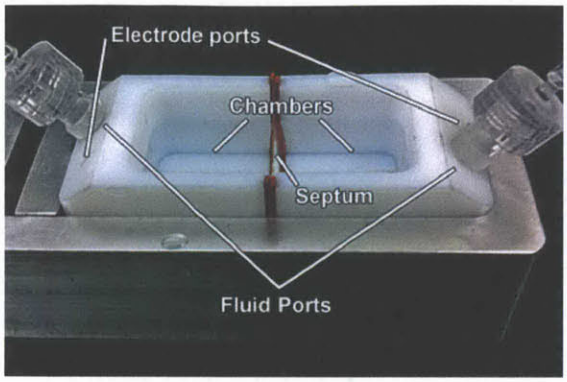

Figure 9: Image of Teflon chamber setup for hydrated lipid bilayer formation.

Teflon and polycarbonate were used as possible septum materials. Both are hydrophobic and are suitable for monolayer folding. Teflon sheets of 25 μm thickness and polycarbonate sheets of 20 μm thickness purchased from Goodfellow were cut to size using a razor blade. All parts were subject to ultrasonic cleaning in ethanol where materials are often heated to around 50°C. After cleaning, Teflon was noticed to suffer annealing as evidenced by slight indentations due to compression from the gaskets. Also, Teflon partitions tended to warp much more easily. These effects are likely due to a much lower Young's modulus and yield strength of Teflon compared to polycarbonate.

Both septum materials were used to test two different aperture formation methods: hot needle and laser ablation. The hot needle approach involves puncturing and melting the partition with a heated needle point. A tungsten probe tip was heated using a soldering iron and carefully placed in contact with the partition. While this method is rather simple, the quality of holes was not sufficient for lipid bilayer formation. As shown in Figure 10a, the hot needle did not leave a clean cut around the edges. In addition, there is very little control of the size of the aperture, which is important for experimental repeatability. Laser ablation, which is the application of a pulsed laser through a mask defining the aperture shape and size, offers significantly better control in terms of hole size. However, Teflon yielded similar poor aperture quality as shown in Figure 10b while polycarbonate showed nearly flawless results as shown in Figure 10c. This may be due to the fact that Teflon has a higher melting temperature while having similar thermal diffusivity as polycarbonate and is thus more susceptible to diffusion of heat and melting/warping around the edges.

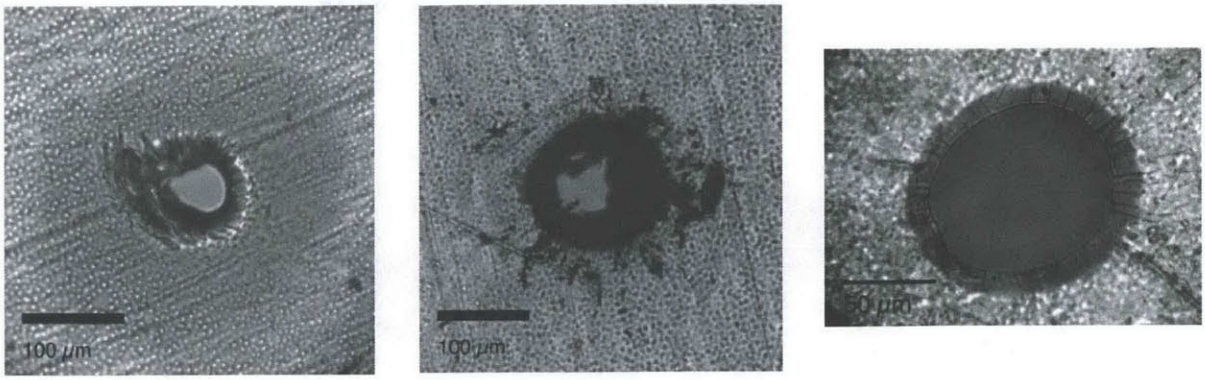

(a) (b) (c)

Figure 10: Optical microscope images of apertures in Teflon and polycarbonate partitions. **(a)** Aperture created by hot needle method on Teflon. **(b)** Aperture created by laser ablation on Teflon. **(c)** Aperture created by laser ablation on polycarbonate.

Outside of the chamber setup, the experimental setup includes a function generator (AFG3101, Tektronix), current amplifier (428-PROG, Keithley), oscilloscope (MSO7104A, Agilent), and two syringe pumps (Harvard Apparatus). All of these instruments are controlled by a computer program via RS-232 and GPIB connections. The function generator supplies a voltage profile across the two Ag/AgCl electrodes while the current amplifier, which is connected in series, measures current. A current amplifier was used as opposed to a multimeter since extremely small currents on the order of nanoamps and highly transient currents with frequencies in to the kHz range were expected. Since a current amplifier only transforms a current signal into a voltage signal, an oscilloscope was used to measure current. Two disposable 60 mL syringes with Luer-Lok connections and 1/6" ID Tygon tubing were used for fluid connections.

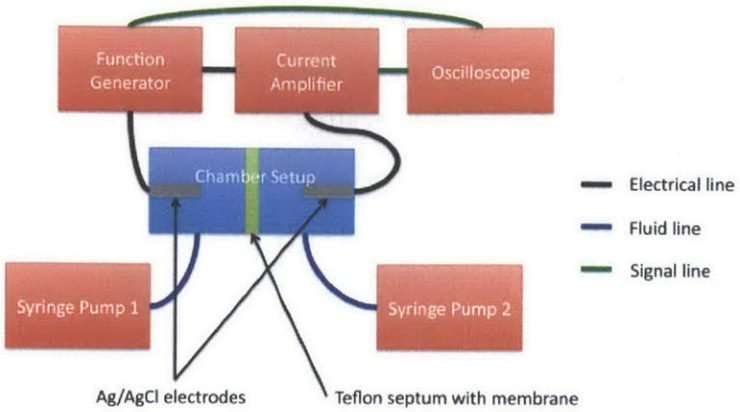

Figure 11: Experimental arrangement of lipid formation chamber, measurement instrumentation and syringe pumps.

To verify that the instrument setup was working properly, and the Ag/AgCl electrodes were indeed symmetric (have no voltage bias when zero potential is applied) and linear in the range of voltages to be tested, a simple conductivity measurement was performed. A range of voltages between -1 and 1 V were applied. The current data was measured and fit to a line according to Ohm's law as shown in Figure 12. The electrolyte solution used was 0.1 M KCl.

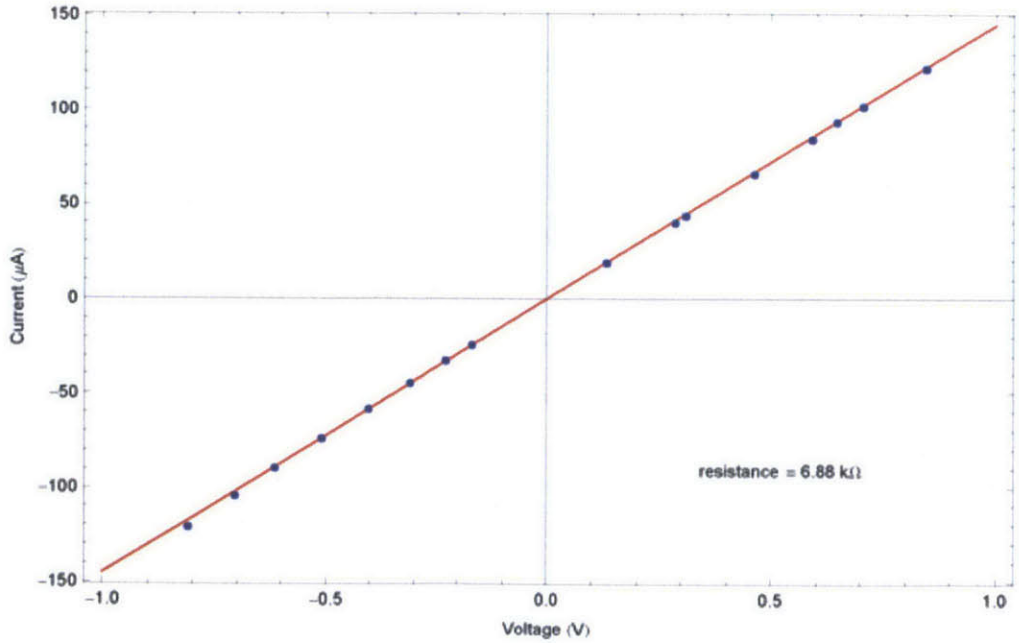

Figure 12: Conductivity across the aperture with 0.1 M KCl solution and Ag/AgCl electrodes

Electroporation Tests

To test electroporation, a voltage ramp test as demonstrated by Kramar et al. [25] was conducted. While previous work has described the usage of voltage pulses to break down the lipid membrane [13, 26], the use of voltage ramp allows for the precise measurement of the breakdown voltage in one run whereas in a pulse based experiment, multiple pulses of different amplitude would have to repeatedly be tried. In the ramp test, the current initially rises based on the conductivity of the bilayer. After the breakdown voltage, the conductivity significantly rises as indicated by a steeper slope. The results of one such test is shown in Figure 13.

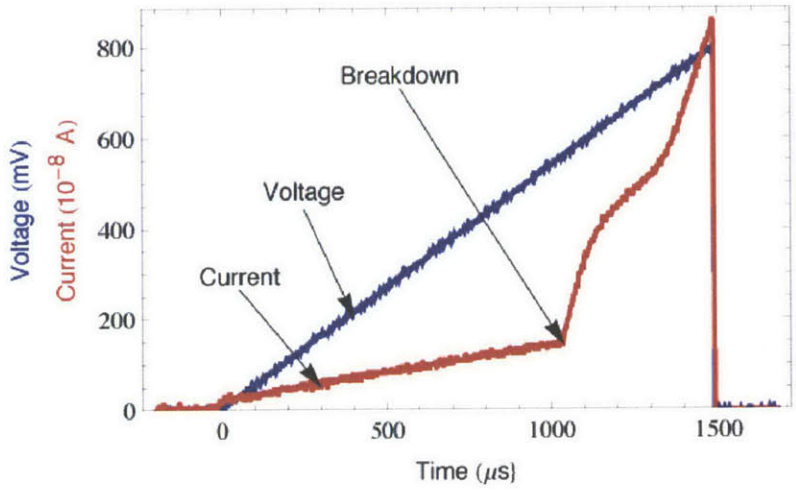

Figure 13: Voltage breakdown of DiPhyPC. After the voltage has reached 600 mV, the conductivity rises significantly.

Before and after the bilayer is electroporated, conductivity measurements are made using a square wave of 50 mVpp amplitude and 5 kHz frequency. The post-electroporation conductivity is always higher than the pre-electroporation conductivity, which indicates that the electroporation was irreversible and that membrane rupture occurred. In fact, post-electroporation conductivities were the same as that in the absence of any membrane.

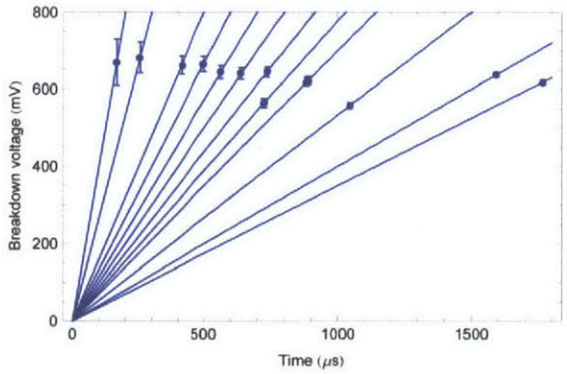

Figure 14: Breakdown voltages for different ramp rates

A range of different ramp rates was also tested to investigate any possible dynamic effects on the breakdown voltage. However, no significant trend or correlation was observable as shown in Figure 14. All breakdown voltages were around 600 mV and this value seems largely independent of ramp rate. The variance in breakdown voltage suggests that breakdown is a probabilistic event. The probability of breakdown may be tied to the Boltzmann probability of a metastable pore in Equation 3. Further experiments and analysis into the distribution of voltage breakdown may shed some light into this issue.

Impedance Spectroscopy

Impedance spectroscopy, which is the measurement of electrical impedance across a range of input frequencies, was conducted for DiPhyPC lipid bilayers. A sinusoidal input of 50 mVpp and frequencies ranging from 25 Hz to 25 kHz spaced logarithmically were used. At each frequency, a waveform of 5 period lengths was sampled. Since the amplitudes ranged two orders of magnitude, samples were taken at several gains to determine the best one to sample at. The resulting sinusoidal current output was least squares fit to determine the amplitude and phase. The resistance and phase of the lipid bilayer as functions of frequency are shown in Figure 15.

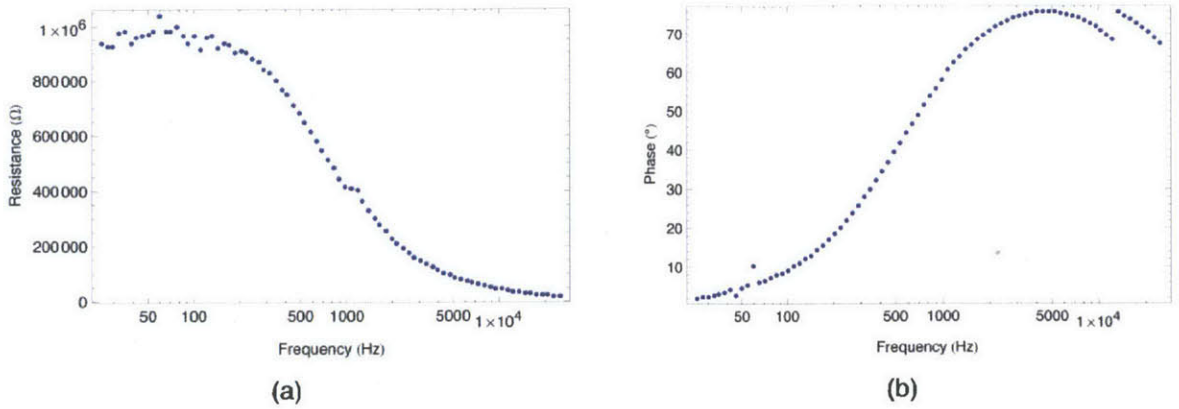

(a) (b)

Figure 15: (a) Resistance of DiPhyPC as a function of frequency. **(b)** Current phase relative to voltage as a function of frequency.

The general trend of decreasing resistance and phase approaching 90° with increasing frequency is consistent with the parallel RC circuit model as shown in Figure 16. The capacitance is due to the fact that when a potential is applied, a charge concentration of opposite sign forms along the membrane in the form of an electric double layer. At low frequencies, the capacitor behaves as an open circuit; thus, the overall resistance becomes $R_{\text{electrolyte}} + R_{\text{membrane}}$. At high frequencies the capacitor behaves as a short circuit; thus, the effective resistance becomes $R_{\text{electrolyte}}$. Furthermore, the current phase becomes 90° ahead of the voltage in phase. The fact that phase never actually reaches 90° in Figure 15b, but starts dipping lower is likely due to limitations of the current amplifier. At higher frequencies, the effect of the nonzero rise time becomes more important. The vertical shift in phase is due to a change in gain setting where each gain setting has different rise time characteristics.

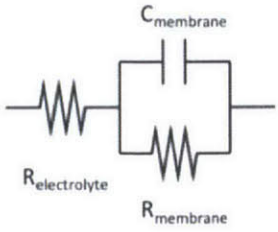

Figure 16: Electric circuit model for the lipid bilayer in electrolyte solution.

In order to qualitatively compare the impedance behavior of the bilayer in comparison to an ideal electrical circuit, we can use complex impedance. We use phasors to represent complex impedance as

$$Z = \frac{V_{pp}\, e^{-i\phi}}{I_{pp}} \qquad \textbf{Equation 14}$$

where Z is the complex impedance, V_{pp} is the peak-to-peak voltage, I_{pp} is the peak-to-peak current and ϕ is the phase. A plot of the real and imaginary parts of Z for each data point is shown in Figure 17. The ideal parallel RC circuit behavior is a semicircle with intercepts on the real axis at $R_{electrolyte}$ and $R_{electrolyte} + R_{membrane}$.

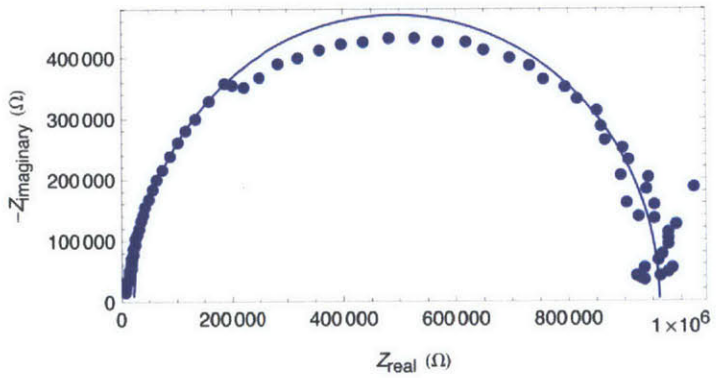

Figure 17: Complex impedance of DiPhyPC membrane with overlaid over ideal parallel RC behavior (semicircular solid line).

Summary

Fully hydrated lipid bilayers are desired in order to demonstrate the electroporation effect. To form fully hydrated lipid bilayers, a Teflon chamber setup was built. Different aperture creation methods and partition materials were tested and laser ablated polycarbonate were found to be the highest quality. The chamber is connected in an electrical loop by two Ag/AgCl electrodes where potential is controlled by a function generator and current measured by a current amplifier/oscilloscope setup. Electroporation was observed by simple breakdown tests using a voltage ramp. No correlation between ramp rate and breakdown voltage were found. Impedance tests performed verified the parallel RC behavior of the lipid bilayer. These tests are the basis for future experiments in characterizing electroporation behavior of different lipids.

Chapter 3: Supported Lipid Films

Lipid Bilayer

Deposition by Vesicle Fusion

Supported lipid films differ from fully hydrated bilayers in that they are in contact with a solid substrate and may or may not be in contact with water. For supported lipid bilayers with outward facing heads, a hydrophilic substrate must be used such that the polar heads can adhere to the surface. There are two main methods to deposit lipid bilayers: Langmuir-Schaefer and vesicle fusion methods. Langmuir-Schaefer involves first depositing a monolayer by Langmuir-Blodgett method (which will be described later) and then holding the substrate horizontally and allowing it to touch the surface as shown in Figure 18a. The vesicle fusion technique involves preparing a hydrated vesicle solution and depositing on top of the substrate. Due to polar interactions between the heads and the hydrophilic substrate, vesicles will naturally adsorb to the surface. Below a critical vesicle size, vesicles fuse together and grow. Once vesicles reach the critical size, they spontaneously rupture and form a bilayer patch on the substrate as shown in Figure 18b. The key to this procedure is that the temperature should be above gel-fluid transition temperature so that the lipid is laterally mobile (lipids are free to move along the plane of the bilayer). This allows fusion to occur and vesicles to rearrange themselves on the substrate.

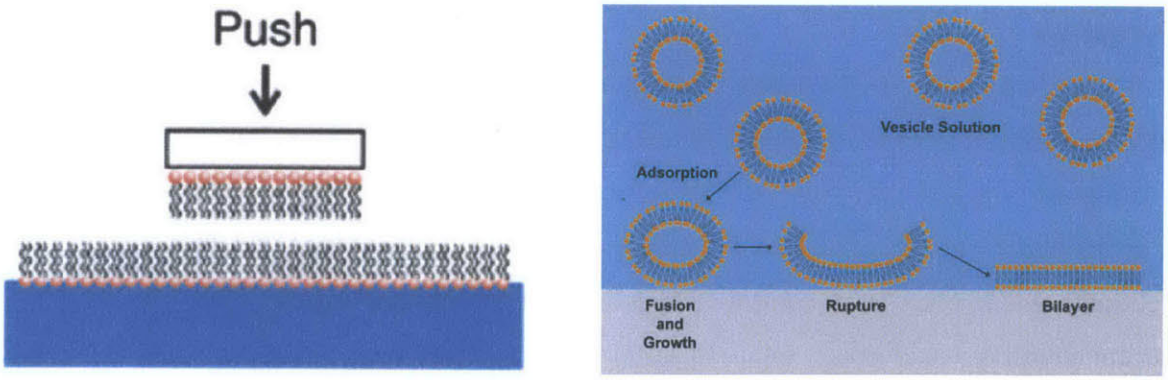

Figure 18: (a) Langmuir-Schaefer technique of bilayer deposition [27]. **(b)** Vesicle fusion method of lipid bilayer deposition.

Pure dried DPPC powder is combined with a buffer solution at a concentration of 0.1 mg/mL. The buffer solution is 0.05 M KCl, 0.005 M HEPES and drops of NaOH to bring the pH to 7.5. The mixture is placed in a 4 mL vial and is mixed in the vortex of stirred water in a flask heated at 50°C (above $T_{transition}$ = 41°C) by a hot plate. The lipid is left in this hydration process for 30 minutes. The solution is then transferred to a glass 100 μL syringe and attached to an Avanti mini-extruder with an identical return syringe attached to the other end. The extruder holds a polycarbonate track-etch membrane with 100 nm diameter pores. The lipid solution is then passed through this membrane ten times to form 100 nm diameter vesicles. Throughout this entire process, the extruder sits on top of a hot plate so that the lipid stays in the fluid state. The resulting vesicle solution is then deposited into a small Petri dish in which a silicon substrate sits. The lid to the Petri dish is then closed to induce saturation and prevent evaporation. The Petri dish is placed on top of the hot plate for 30 minutes to allow for vesicle fusion deposition to occur.

AFM Characterization of Surface Coverage

The quality of lipid bilayer coverage was characterized using AFM (Dimension 3100, Veeco). Tapping mode tips (RTESP, Bruker) of 42 N/m spring constant were used. When samples were exposed to air after deposition, it was found that complete coverage was unattainable. Bilayer patches covered the surface as shown in Figure 19a. The fact that heights of these patches correspond to twice the height of DPPC molecules (~ 5 nm) is strong evidence that these patches are in fact lipid bilayers. In order to determine whether full coverage is in fact attainable, a sample was observed using AFM fluid contact mode imaging. Softer silicon-nitride tips of 0.07 N/m spring constant (MLCT, Bruker) were submersed in the same buffer solution used during vesicle fusion deposition. Care was taken not to expose the sample to air; however, some exposure for a few seconds while transferring the sample to the AFM sample holder was unavoidable. Despite this, the surface showed more coverage (Figure 19b). Instead of patches, holes or voids are present where the bilayer is not covering the underlying substrate. The depth of these holes corresponds to twice the height of a DPPC molecule, which proves that a bilayer structure is in fact covering the surface.

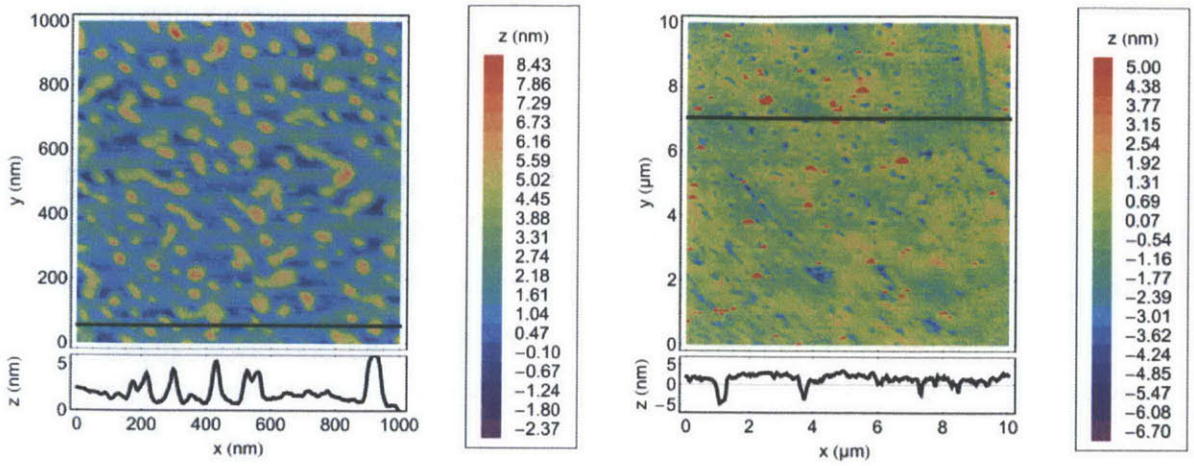

(a) (b)

Figure 19: AFM height profile of DPPC bilayer on silicon **(a)** after exposure to air and **(b)** unexposed to air and imaged in fluid. Step heights correspond to the thickness of the bilayer (~ 5 nm).

Wetting on Lipid Bilayer

Since lipid bilayers are unstable in air, a sessile drop test is not possible. Even with the partially covered substrates, however, the samples were observed to be completely wetting. This indicates the presence of lipid bilayers on the substrate as they are more hydrophilic than silicon, which has a contact angle of about 37°. A completely wetting surface cannot provide a quantitative measure of surface energy. Because of this, we plan to perform a test, as shown in Figure 20, as part of future work. The lipid bilayer will be completely immersed in an aqueous solution and an immiscible high density oil will be used as a probe liquid.

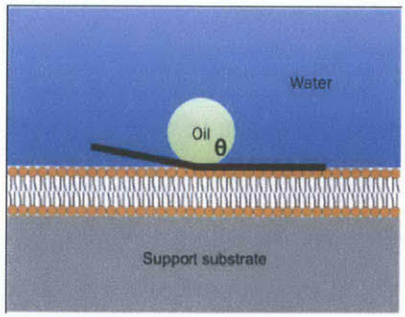

Figure 20: Proposed method of characterizing interfacial surface tension of lipid bilayer.

Lipid Monolayer

Deposition by Langmuir-Blodgett

Langmuir-Blodgett is a technique invented by Irving Langmuir and Katherine Blodgett to deposit surfactant molecule films on substrates by one molecular layer at a time. Since surfactants sit at the air-water interface, this technique uses the meniscus of a passing substrate to gradually place molecules on the substrate. This can be done either with a hydrophobic substrate pushed into the liquid or with a hydrophilic substrate pulled out of the liquid, the latter of which is shown in Figure 21. Since the last step in any deposition process requires pulling the substrate out of the liquid, the number of possible layers is odd for a hydrophilic substrate (1, 3, 5, 7, etc.) and even for a hydrophobic substrate (2, 4, 6, 8, etc.).

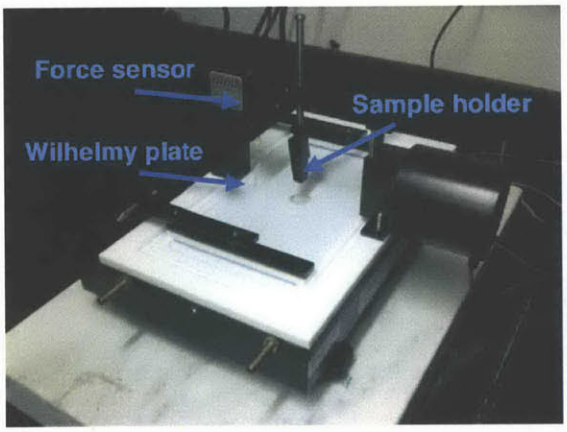

Figure 21: Langmuir-Blodgett trough.

A paper or platinum Wilhelmy plate is used to monitor surface pressure, which is the loss in surface tension due to the presence of a surfactant. As the concentration of lipids increases on the lipid-vapor interface, the surface pressure increases as shown in Figure 22. This change in surface pressure is mainly an effect of decreased contribution of high surface tension water and increased contribution of the lower surface tension tails as the lipid density increases. The surface pressure can be defined as

$$\Pi = \gamma_{water} - \gamma_{monolayer} \qquad \textbf{Equation 15}$$

where $\gamma_{monolayer}$ is the apparent surface tension of the liquid. This apparent surface tension is determined from

$$\gamma_{monolayer} = \frac{F}{P\cos(\theta)} \qquad \textbf{Equation 16}$$

where F is the force exerted on the Wilhelmy plate, P is the wetted perimeter, and θ is the contact angle of the liquid on the Wilhelmy plate. Since our plate is porous and wicking, this angle is taken to be 0°. The surface pressure-area isotherm shown in Figure 22 shows different regimes or phases based on packing density. In the low density limit, the lipids behave as a two-dimensional "gas." In the intermediate density range (70-110 $Å^2$/molecule), a distinct "liquid" phase emerges. In the high density range, a "solid" crystalline packing of lipids occurs. Once the density becomes too high (< 50 $Å^2$/molecule), however, the lipid film begins to collapse into the solution.

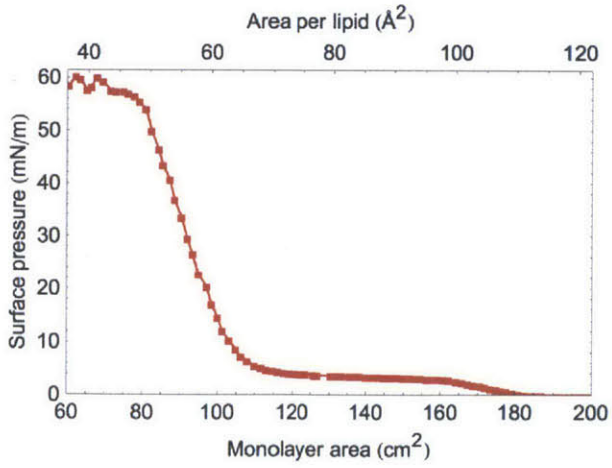

Figure 22: Surface pressure-area isotherm of DPPC.

Langmuir-Blodgett deposition is performed on a Langmuir-Blodgett trough (601, NIMA) as shown in Figure 21. Approximately 170 mL of DI water is deposited into the trough. The Wilhelmy plate is placed on the load cell and lowered into the fluid. After waiting several minutes for water to completely wick up the plate, the surface pressure is zeroed. A surface pressure-area isotherm is performed before adding of any lipids to ensure that no contaminants are present. The substrates are square glass coverslips with 18 mm sides. These are rinsed with

ethanol, acetone and DI water, after which they are plasma cleaned in an oxygen or argon environment. The contact angle of these plasma cleaned substrates is 0°, *i.e.*, they are completely wetting. These are then loaded into the sample holder and lowered into the trough until the water level is just beneath the holder. Since the sample holder grips the sample by a simple clamping mechanism, the substrate is not completely submerged. 20 mL of 1.91 mg/mL DPPC in heptane is added to the liquid-vapor interface. Care is taken not to let drops fall on to the surface; rather, drops are allowed to come in contact with the liquid and spread about. This way, the absorption of lipids into the water and formation of vesicles is minimized. The setup is left for five minutes in order to let the heptane evaporate off. The Teflon barriers are then closed at a rate of 20 mm^2/minute until a target surface pressure is reached. An internal feedback mechanism adjusts the area in order to maintain this target surface pressure. The lipid is left to equilibrate for 1 hour after which the substrate is raised out of the surface at a rate of 5 mm/minute to deposit lipid monolayers onto both sides of the substrate.

Contact Angle Tests on Lipid Monolayer

The wetting behavior of the lipid monolayer was qualitatively checked by placing a droplet of water at the boundary between the monolayer coated and uncoated regions. It was found that the water preferentially wetted the uncoated, hydrophilic substrate. This showed that the monolayer coating renders the substrate more hydrophobic as expected since the tails should be sticking outward.

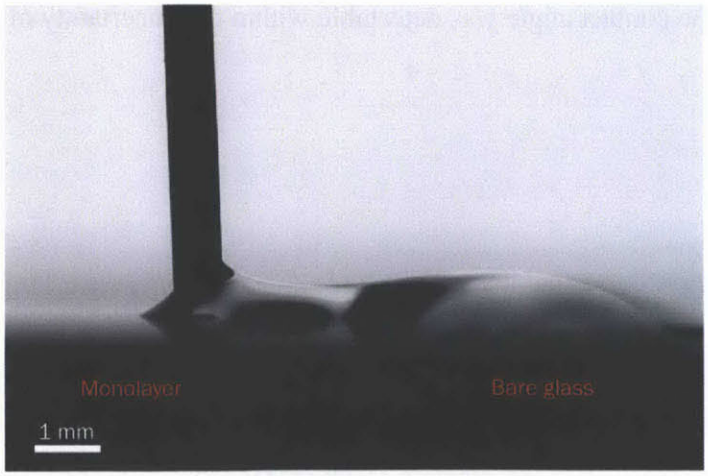

Figure 23: Preferential wetting of the bare glass region as opposed to the more hydrophobic monolayer coated region.

Contact angle measurements with sessile water drops were also conducted on the lipid monolayer coated glass. Advancing and receding contact tests were conducted by the syringe method. Contact angles were attained using the DropSnake plug-in for ImageJ. The contact angles were about 60 degrees in the advancing state and about 30 degrees in the receding state as shown in Figure 24.

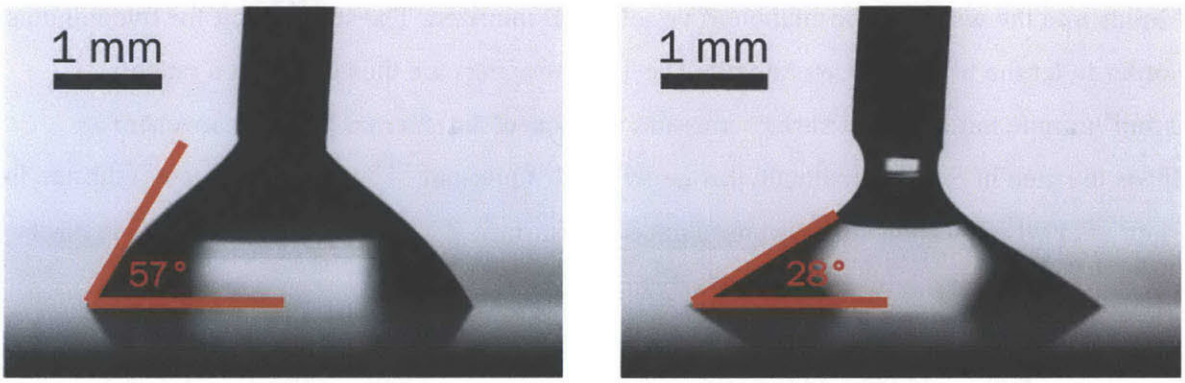

(a) (b)

Figure 24: Contact angle of water on DPPC monolayer on glass **(a)** in the advancing state and **(b)** in the receding state.

The effect of using different target surface pressure during Langmuir-Blodgett on the contact angle was investigated. By varying surface pressure, we anticipated that the packing density would change and thereby the surface energy would change as well. However, no apparent change in the contact angle was detectable within the uncertainty of measurements as shown in Figure 25.

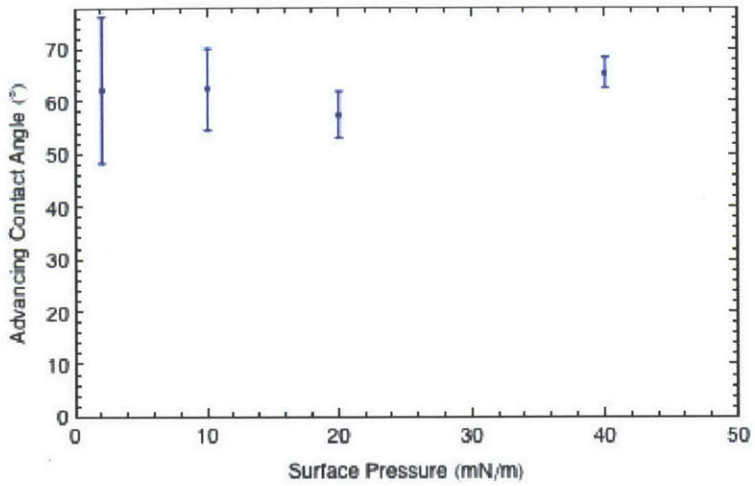

Figure 25: Lack of effect of surface pressure on the advancing contact angle of water on DPPC monolayer on glass

Furthermore, the overall contact angles are not in agreement with Cross *et al.* [28] who used similar lipid films on glass and reported a contact angle of 95°. However, they did not report their substrates to be plasma cleaned. Since the plasma cleaning renders the glass as completely wetting, it was thought that this figure could be reproducible if substrates were only cleaned with solvents. Indeed, depositing on non plasma cleaned glass yielded advancing contact angles close to 90°.

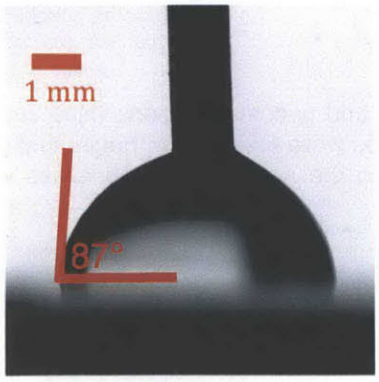

Figure 26: Near 90° contact angle of non plasma cleaned glass.

AFM Characterization of Lipid Monolayer Films

In order to verify the surface coverage of lipid monolayers on glass, phase information from AFM tapping mode was used to measure differences in the interactions between the coated

and uncoated regions. The phase is the phase shift between the oscillating cantilever and the input drive signal. This is highly dependent on the interaction between the tip and the surface material; thus, it is a good way to distinguish between bare glass and monolayer coated glass. Eight different spots oriented on a line perpendicular to the coated and uncoated boundary were imaged as shown on the left hand side of Figure 27.

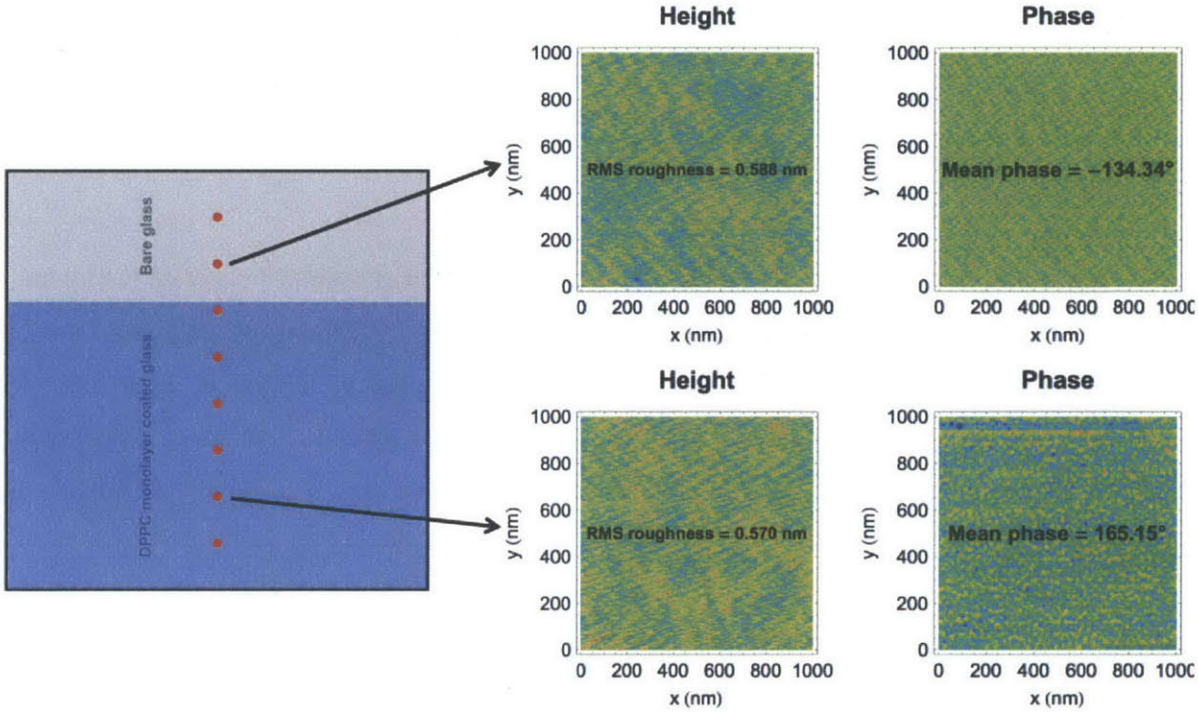

Figure 27: Sample showing coated and uncoated regions (blue and gray respectively) on the left. Red dots signify points where AFM images were taken. AFM height and phase profiles from the second from top and bottom points are shown on the right. The roughnesses were similar while the phases were drastically different.

While both bare glass and the DPPC monolayer had similar RMS roughnesses of about 0.6 nm, their phases were completely different. The similarity in roughness indicates that the lipid monolayer conforms to the roughness of the underlying glass. These measurements were consistent for the region in which they were taken as show in Figure 28.

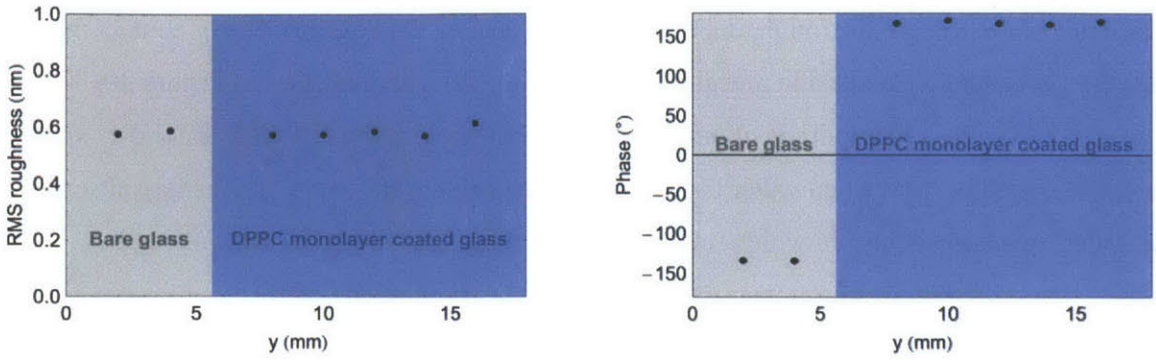

(a) (b)

Figure 28: (a) RMS roughness and **(b)** phase for different points on the partially coated glass substrate

AFM was also used to investigate the reason for the large hysteresis on the contact angle (~ 30°) was observed. Using phase imaging, features resembling crystal grain boundaries were observed as shown in Figure 29a. A droplet of DI water was then placed on the substrate and allowed to evaporate off. The same spot was then imaged and showed a completely different phase landscape as shown in Figure 29b. These results suggest that the water is interacting with the monolayer and substrate such as to rearrange or displace the lipids.

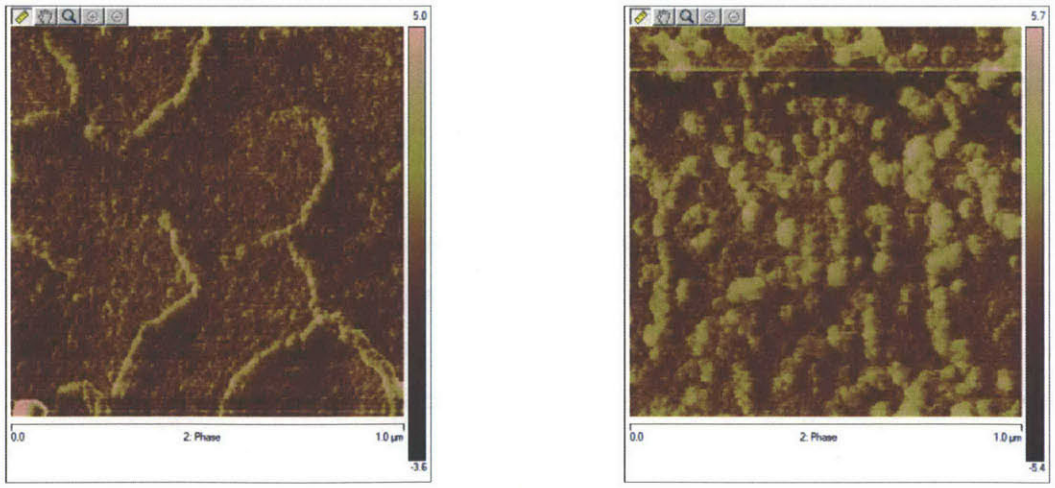

(a) (b)

Figure 29: AFM phase image of DPPC monolayer on glass **(a)** before and **(b)** after exposure to water.

Characterizing the unwetted surface using contact mode AFM showed that numerous defects exist on the monolayer surface. These circular voids are due to vesicles that are adsorbed to the surface while the sample is submerged inside the liquid before deposition. As the lipid is

raised out of the Langmuir trough, deposition occurs around the vesicles. Using contact mode, the vesicles can be pushed aside revealing the defect underneath as shown in Figure 30. These voids span from tens to hundreds of nanometers in diameter and are typically around 1 nm in depth. It is possible that when water comes in contact with the surface, vesicles may absorb into the water, revealing a void in which interaction with the underlying glass may occur.

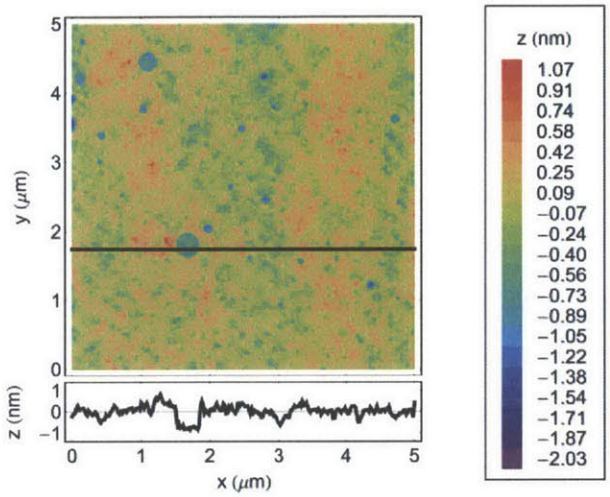

Figure 30: AFM contact mode image of circular voids from which vesicles were originally located on the DPPC monolayer coated glass.

Wetting of Small Droplets

Since the voids are spaced approximately several microns apart, an attempt was made to see whether the contact angle of water was higher at smaller drop sizes. If droplets are small enough, they are less likely to be in contact with any vesicles and potentially have significantly less interaction with the underlying glass. A simple test was conducted where a small humidifier unit with a piezo-electric diaphragm was used to deposit a mist of droplets on the surface. The surface was monitored with an optical microscope. Immediately after transfer to the surface, small droplets on the order of one micron began to form (Figure 31a). However, as more droplets were transferred from the mist, droplets began to coalesce together (Figure 31b). From the initial point of transfer, it is difficult to infer the contact angle of all the droplets. However, it is known that at least some of them are not hydrophobic since non circular droplets appear. Hydrophobic droplets should appear perfectly circular. After droplet coalescence has occurred, it is apparent that all droplets are not hydrophobic from the non-circular shapes.

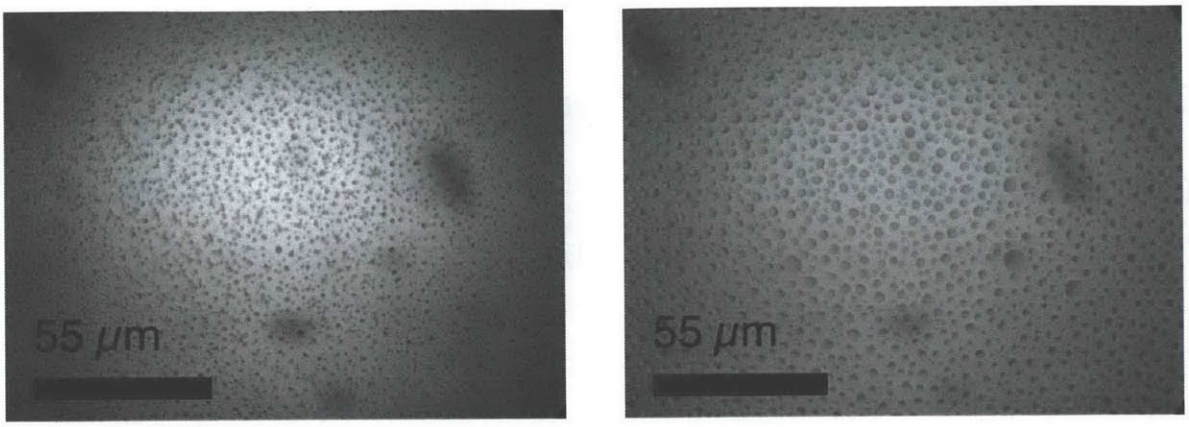

(a) (b)

Figure 31: Water on droplets on DPPC monolayer coated glass **(a)** immediately after droplet transfer, **(b)** after droplets coalesce together.

Summary

Supported lipid films allow for a study of independent tail and head surface energies by sessile drop contact angle measurements. Bilayers were formed by vesicle fusion but were found to be unstable in air. Monolayers were formed by Langmuir-Blodgett deposition where surface pressure can be varied. With glass as a substrate, contact angles were determined in the advancing and receding states. Using AFM, the monolayer coverage was verified and water was found to interact with the underlying glass substrate. Using a small humidifier, an attempt to observe small droplets with higher contact angle was made; however, due to resolution limitations, no conclusive evidence of higher contact angle droplets were found. The basic procedure of droplet wetting on lipid monolayers outlined in this chapter was used in the next set of experiments with mica substrates and three probe liquids (water, formamide, and diiodomethane).

Chapter 4: Detailed Study of Monolayer on Mica

Mica as a Substrate

After initial testing of lipid films described in Chapter 3, it was found that there were several challenges. For the lipid bilayer, formation of a uniformly covered lipid bilayer was difficult because of its instability in air. With the lipid monolayer, contact angles were low and exhibited high hysteresis. Since glass, which was used in monolayer formation, is amorphous and has a finite roughness (~ 0.6 nm), it was thought that using an atomically smooth, crystalline substrate may yield better results. Hence, mica was chosen since freshly cleaved mica is atomically smooth, crystalline, and hydrophilic. The contact angle of water on mica is 0°. The highest V-1 grade mica (SPI) was obtained in square pieces with a side length of 15 mm. Mica was cleaved using a razor blade and used immediately. DPPC monolayers were deposited as described in Chapter 3.

Structure of DPPC Monolayers on Mica

When different surface pressures were used for deposition of DPPC, AFM showed that the structure of the lipid monolayer changed drastically. While above a surface pressure of 30 mN/m, coverage was mostly uniform. At lower surface pressures however, defects in the form of fragmenting and crystalline cracks became apparent. Because of this effect, wetting experiments were conducted at a high surface pressure of 35 mN/m (unless otherwise stated).

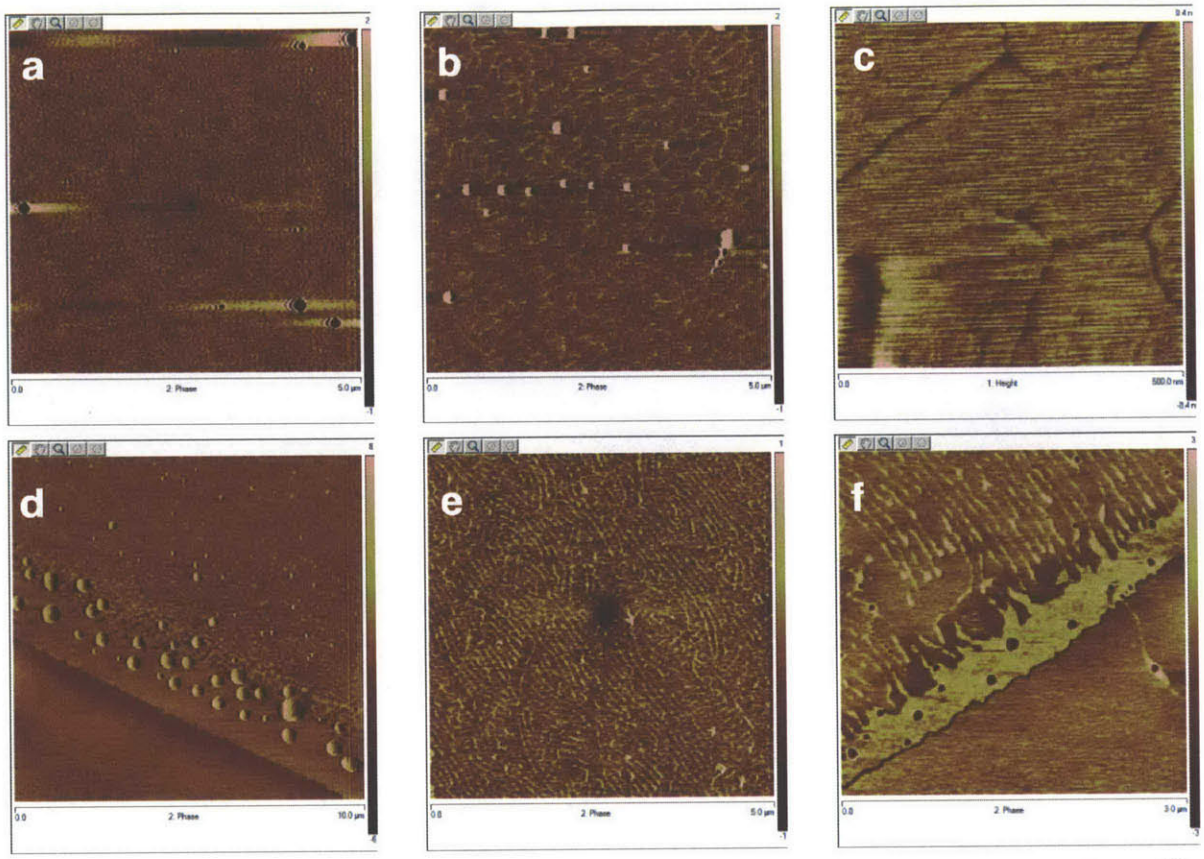

Figure 32: (a) Phase image of DPPC monolayer deposited on mica with a surface pressure of 35 mN/m. At this surface pressure, the coverage is mostly free of defects other than adsorbed vesicles, which are shown as dark circles. Horizontal streaks around these circles are artifacts from flattening each scan line about a mean value. **(b)** Phase image at 25 mN/m. Defects from cracks begin to appear. **(c)** A magnified height image of these cracks. At these crack boundaries, the height is lower, indicating a void. Boundaries tend to be straight with fixed angles suggesting that the lipids are packed in a crystalline structure. **(d)** Phase image of the boundary between uncoated and coated regions at 25 mN/m shows that the crystal crack defects begin from the very start of deposition. **(e)** Phase image at 15 mN/m shows a completely different structure where lipids are in streaks. **(f)** Phase image of uncoated and coated boundary at 15 mN/m shows that streaks begin at the start of deposition.

Water on Mica

Wetting Experiments of Water on DPPC Monolayer Coated Mica

Compared to glass, mica exhibited much higher contact angles initially as shown by Figure 33. These contact angles, however, decrease over time. The initial development of the contact angle is exponential as shown in Figure 34a. After the contact angle has relaxed, it proceeds to decrease linearly with time as a result of droplet pinning and evaporation. From Figure 34c, it is apparent the droplet becomes pinned after relaxation since the base area does not

change after it settles to value around 2.7 mm^2. Meanwhile, the volume of the droplet linearly decreases with time as is expected during evaporation.

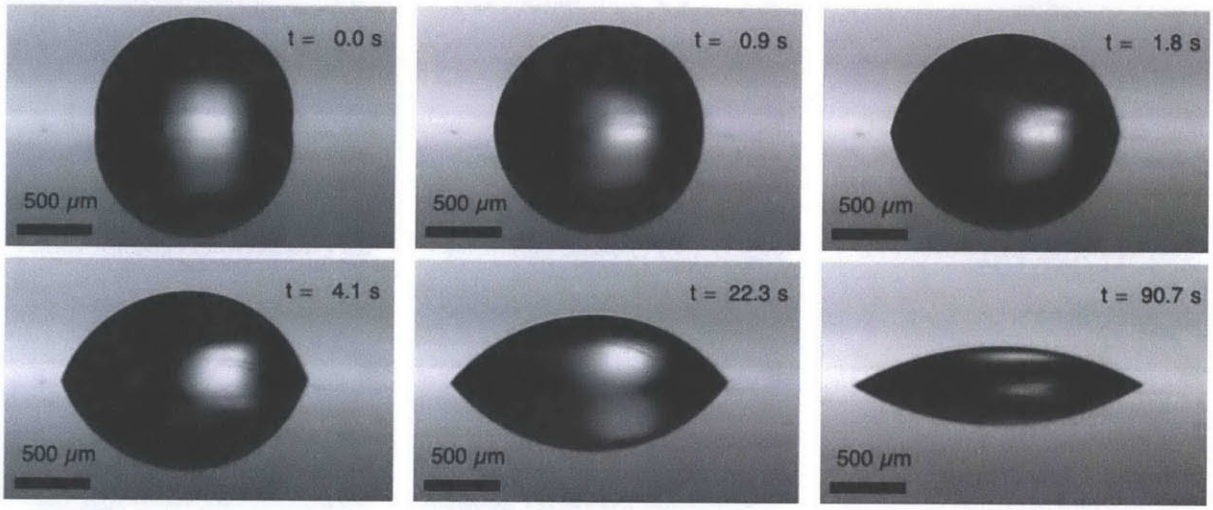

Figure 33: Droplet shape of water on DPPC monolayer coated mica.

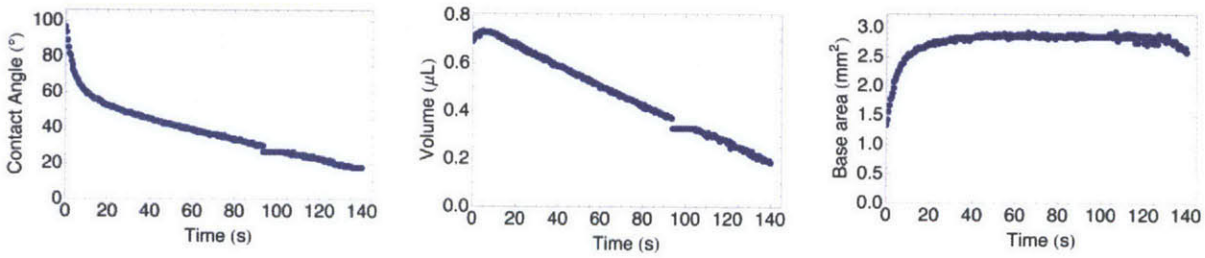

(a) (b) (c)

Figure 34: (a) Contact angle, **(b)** volume, and **(c)** base area of a water droplet on DPPC monolayer coated mica over time.

With this same experiment, the effect of surface pressure on the relaxation behavior or initial contact angle was investigated. Lipid monolayers were deposited at surface pressures of 45, 35, 25, and 8 mN/m. The results of relaxation experiments are shown in Figure 35 and Figure 36. In all cases, the contact angle starts initially high and ranges from 93-102°. The behavior is as stated before where relaxation, pinning and evaporation occur. When the initial contact angle is plotted with the surface pressure as shown in Figure 37a, a weak dependence is observable. However, it is possible that this small trend could be within the uncertainty of measurements. We can conclude that either the surface pressure is not a good indication of the actual packing density of lipids or that the packing density is weakly dependent on the overall surface energy.

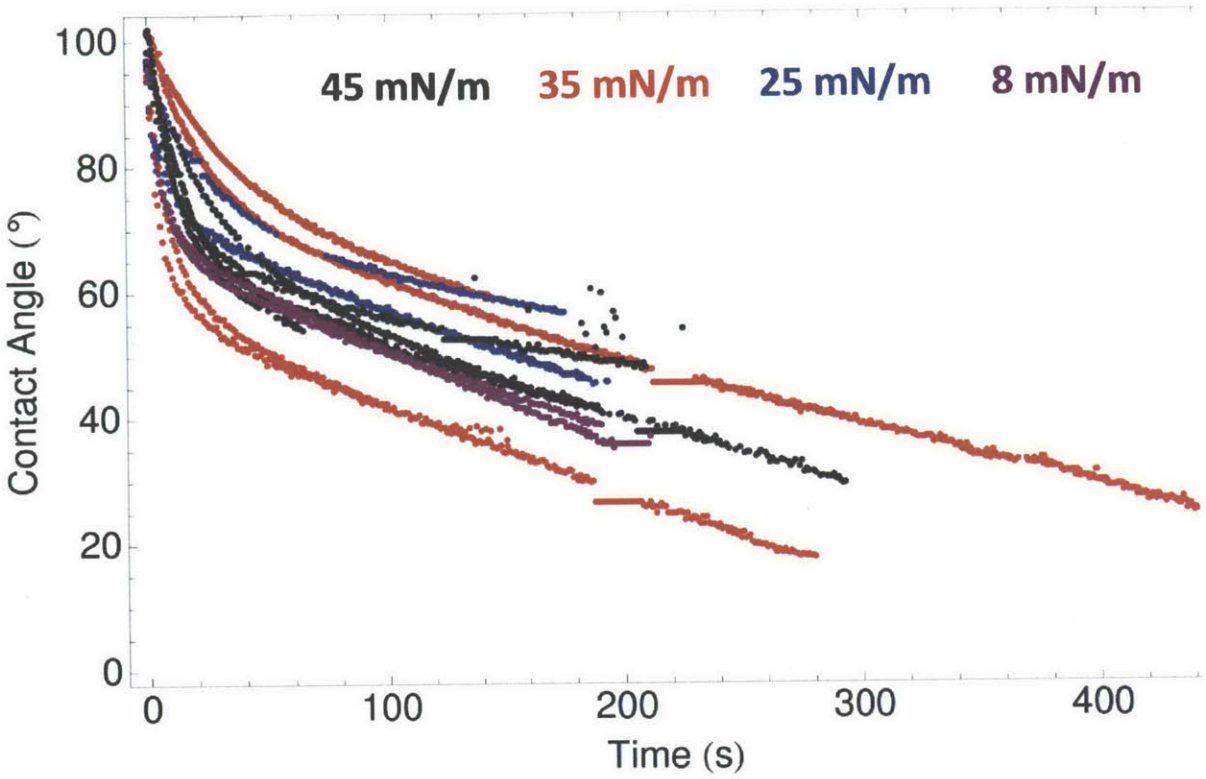

Figure 35: Development of contact angle of water droplets on DPPC monolayer coated mica at various surface pressures.

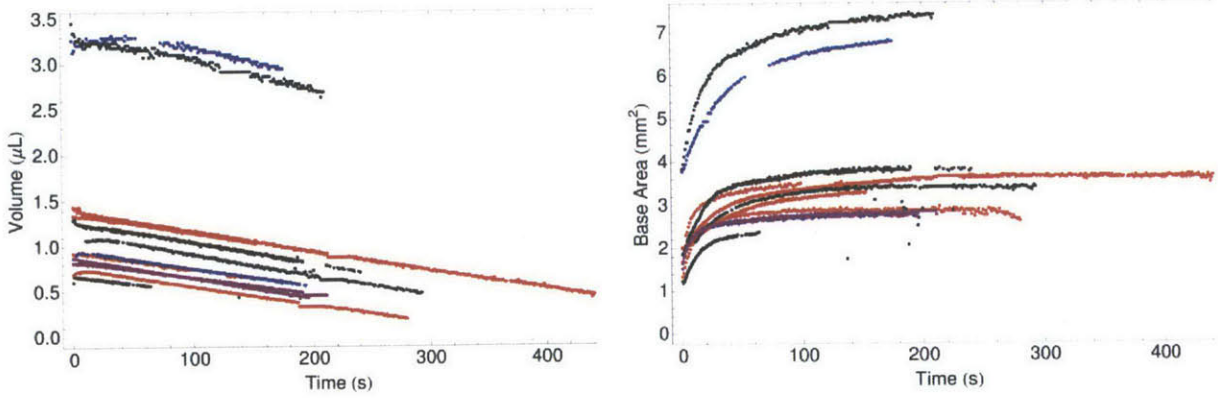

Figure 36: (a) Volume and **(b)** base area of water droplets on DPPC monolayer coated mica at various surface pressures

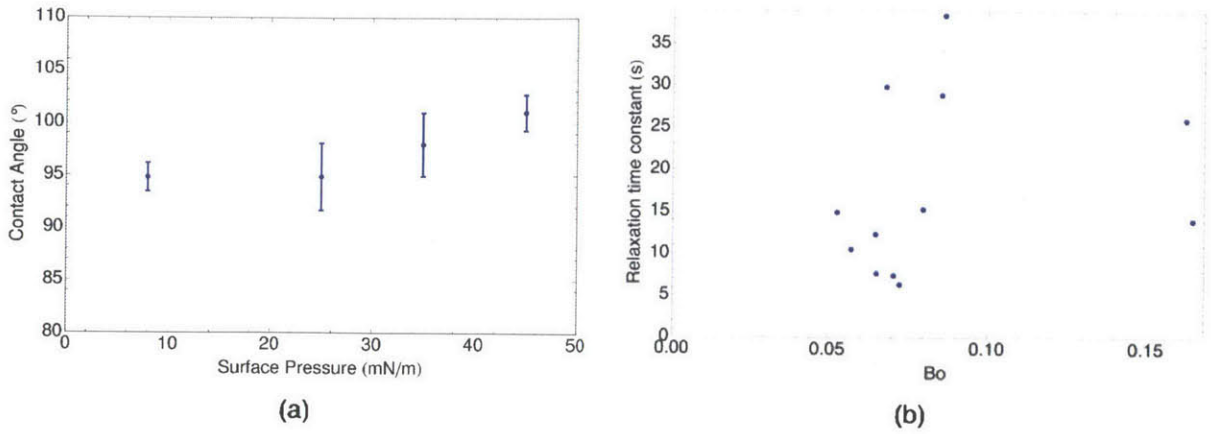

Figure 37: (a) Contact angle of water on DPPC monolayer on mica as a function of surface pressure. **(b)** Relaxation time versus Bond number.

Relaxation is likely due to interactions between the water and the underlying mica substrate, not unlike the high hysteresis observed on glass. One possible mechanism for water to interact with the mica is that water is pulling vesicles off the substrate, exposing the bare mica underneath. If this is true, then the adsorption of vesicles may be a diffusion limited process during the relaxation period. If the diffusivity is constant (valid for dilute solutions), then the relaxation time constant should be proportional with the square of a characteristic length scale ($D \sim L^2/t$). One convenient dimensionless parameters that depends on the square of characteristic length is the Bond number

$$Bo = \frac{\Delta\rho\, g\, R^2}{\gamma_{water}} \qquad \textbf{Equation 17}$$

which is calculated using the initial droplet contact radius. From Figure 37b, it is uncertain whether such a proportionality between Bond number and relaxation time exists. In the two outlying points with high Bond number, the effects of gravity may have become important.

AFM Characterization

Similar to glass substrates, AFM has shown that water interacts with the underlying mica substrate and rearranges and/or displaces lipids as shown in Figure 38.

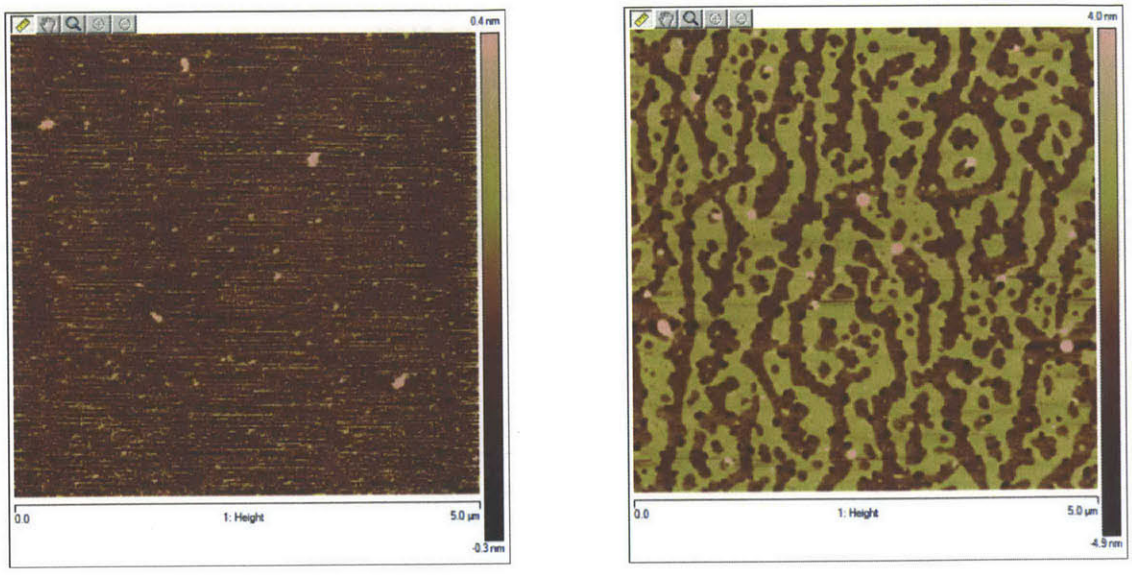

(a) (b)

Figure 38: Height profile of DPPC monolayer coated mica **(a)** before wetting and **(b)** after wetting with water.

Formamide on Mica

Formamide (Figure 39) was another probe liquid used in this study. Formamide is a liquid similar to water in many respects but is more polar (Table 1). Thus, it is assumed that formamide should behave similarly to water, if not show more effects of an interaction with the underlying substrate.

Table 1: Properties of formamide at 20°C

Density (g/cm^3)	Vapor Pressure (mmHg)	Viscosity (10^{-3} Pa · s)	Dielectric Constant	Surface Tension (mN/m)
1.133	0.08	3.3	109.5	58.0

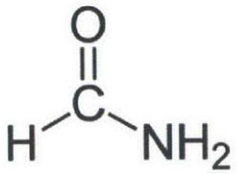

Figure 39: Molecular structure of formamide.

Wetting Experiments of Formamide on DPPC Monolayer Coated Mica

A relaxation test was performed to see whether formamide exhibits the same relaxation behavior as water. The surface pressure of DPPC during deposition was 35 mN/m. A contact angle of around 90° was obtained which, however, remained constant with time. Since the vapor pressure of formamide is very low, no evaporation was observed for the one hour duration of the experiment.

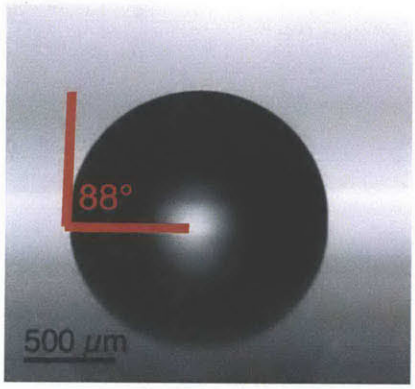

Figure 40: Static contact angle of 88° formamide on DPPC monolayer coated mica which did not change with time.

Since evaporation is so slow, the syringe method was used to measure the contact angle hysteresis. The advancing and receding contact angles of formamide are shown in Figure 41. The contact angle hysteresis was very large and is indicative of some sort of interaction between the formamide and mica. As the contact angle of formamide on bare mica is 0°, it is assumed that the low contact angle is a result of formamide "seeing" the mica, similar to the low contact angles seen during evaporation of water on DPPC monolayer coated mica.

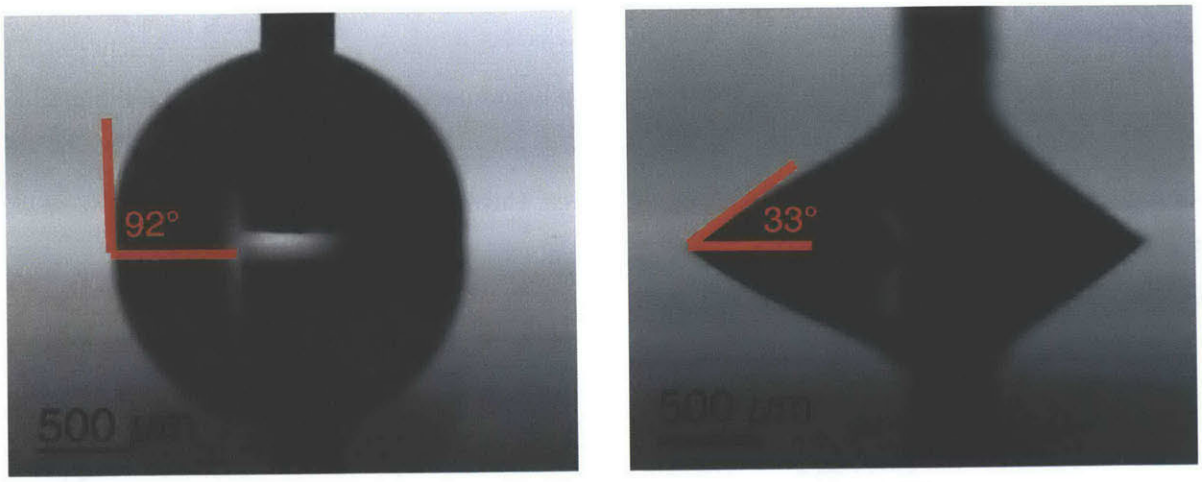

(a) (b)

Figure 41: Contact angle of formamide on DPPC monolayer coated mica in the **(a)** advancing and **(b)** receding states.

AFM Characterization

Similar to water on glass and mica substrates, AFM has shown that lipid rearrangement does occur for formamide as well.

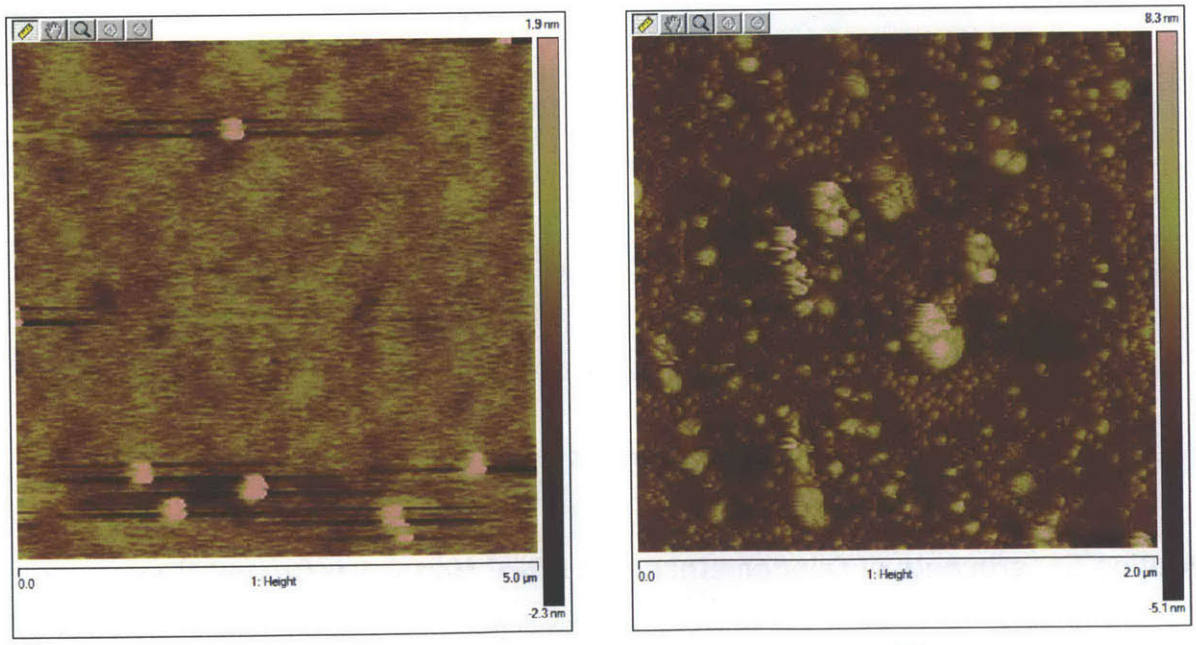

(a) (b)

Figure 42: Height profile of DPPC monolayer coated mica **(a)** before wetting and **(b)** after wetting with water.

Diiodomethane on Mica

Diiodomethane (Figure 43) is the third probe liquid used in this study. Diiodomethane is also similar to water in many respects, however it is almost completely nonpolar (Table 2). It should, therefore, have minimal interaction with mica. Unlike formamide and water, diiodomethane has a nonzero contact angle. The advancing contact angle is 39° while the receding angle is 20° on bare mica as shown in Figure 44

Table 2: Properties of diiodomethane at 20°C

Density (g/cm^3)	Vapor Pressure (mmHg)	Viscosity (10^{-3} Pa · s)	Dielectric Constant	Surface Tension (mN/m)
3.321	0.85	2.8	5.32	50.8

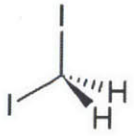

Figure 43: Molecular structure of diiodomethane.

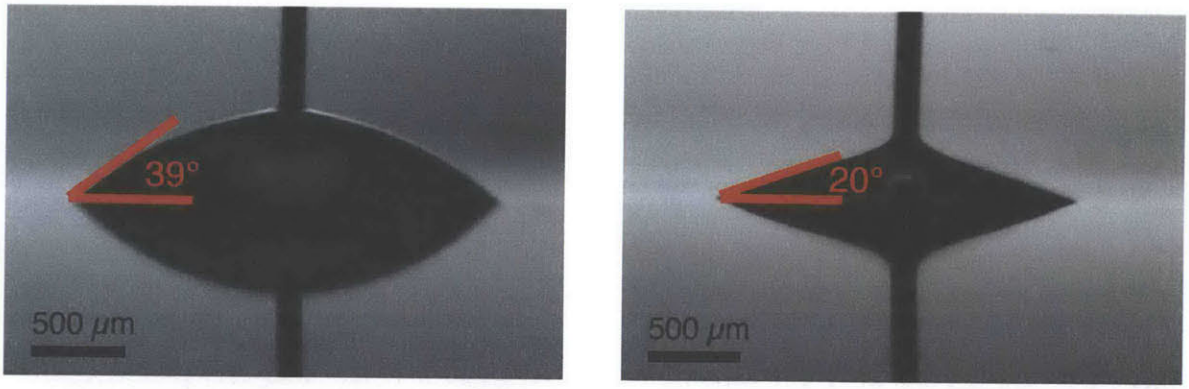

(a) (b)

Figure 44: Contact angle of diiodomethane on bare mica in the **(a)** advancing and **(b)** receding states.

Wetting Experiments of Diiodomethane on DPPC Monolayer Coated Mica

In a static contact angle test where DPPC was deposited at 35 mN/m, diiodomethane exhibited slow but observable evaporation. Like water, evaporation was linear except when the droplet became too small. The base area shrank continuously showing no signs of pinning except

at the very beginning of the test. The contact angle also continuously decreased but slightly irregularly. Towards the end, contact angle dropped rapidly.

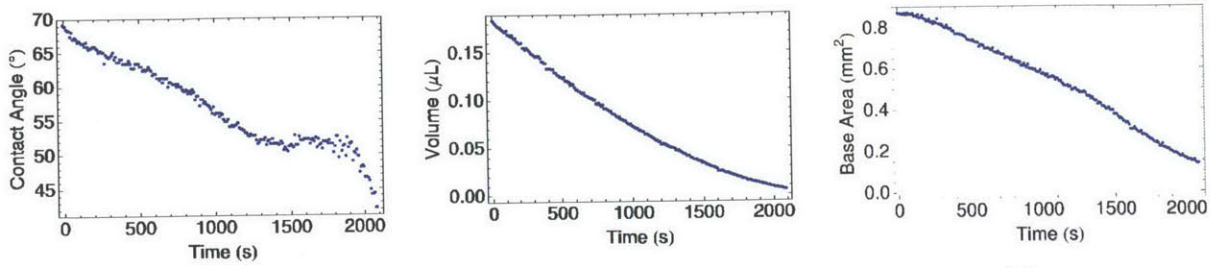

(a) (b) (c)

Figure 45: (a) Contact angle, **(b)** volume, and **(c)** base area of a diiodomethane droplet on DPPC monolayer coated mica over time.

Unlike water and formamide, static contact angles were repeatable even on a previously wetted area. This result suggests that diiodomethane does not interact strongly with the underlying mica substrate, which is most likely due to diiodomethane's low polarity and hence weaker interaction with mica.

The effect of surface pressure on diiodomethane was also investigated where DPPC was deposited at 50, 40, 25, and 15 mN/m. From repeated testing, however, it was found that surface pressure does not change the advancing or receding contact angles. In all cases, contact angle hysteresis of about 10° was observed.

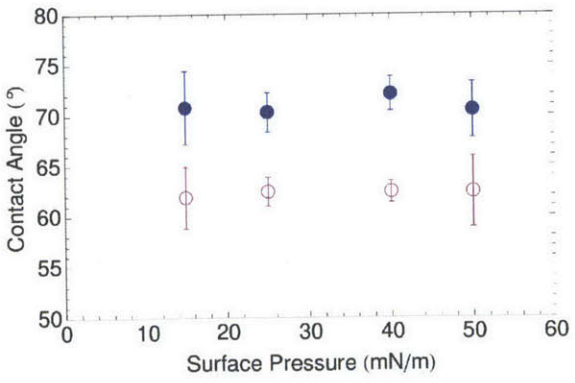

Figure 46: Advancing (•) and receding (○) contact angles of diiodomethane on DPPC monolayer coated mica at various surface pressure.

AFM Characterization

Unlike water and formamide, diiodomethane did not significantly alter the surface of the DPPC monolayer coated mica as shown in Figure 47 in that lipids weren't removed or displaced from the surface. However, the surface tended to have more and smaller vesicles adsorbed to it. Even in the low surface pressure limit, the underlying structure of lipids was unchanged after wetting but an increase of smaller vesicles was observed.

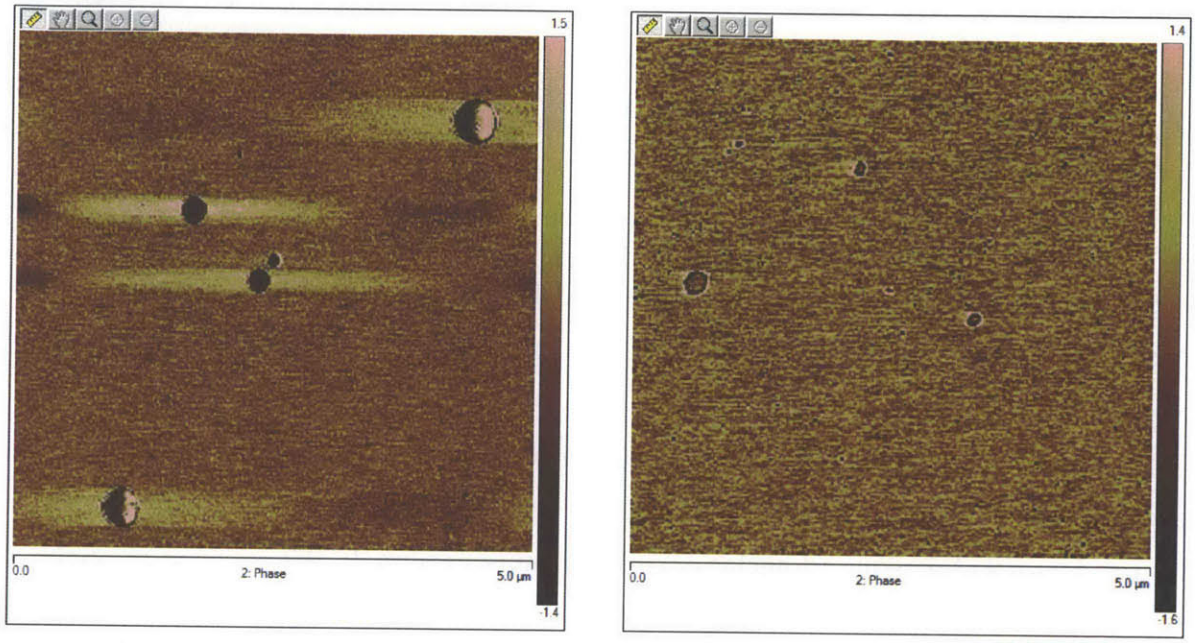

(a) (b)

Figure 47: Phase images of DPPC monolayer coated mica deposited at a surface pressure of 40 mN/m **(a)** unwetted and **(b)** wetted by diiodomethane. Large circles are vesicles adsorbed to the surface.

Summary

In this detailed study of understanding the lipid tail energy, monolayers deposited on mica were tested. The quality of films was noticed to change drastically with surface pressure; however, as long as depositions occurred above 30 mN/m, then coverage was mostly uniform. Three probe liquids were used water, formamide, and diiodomethane for wetting experiments. The two polar liquids (water and formamide) were found to have high contact angle hysteresis and altered the surface morphology of lipids. The nonpolar liquid (diiodomethane) was found to have small contact angle hysteresis and did not alter the surface morphology. In all cases no effect of surface pressure was found.

Chapter 5: Discussion

Probe Liquid Interaction with Underlying Substrate

Both water and formamide, which are polar liquids with high dielectric constants have been shown to interact and alter the surface of DPPC monolayer coated substrates. This interaction has a profound effect on the large hysteresis and small receding angles of these fluids. A concurrent study of this interaction using molecular dynamics (MD) is also being undertaken in our research group (with Dr. Shalabh Maroo) using GROMACS software. In these simulations, DPPC molecules are arranged on a 12 nm x 12 nm quartz substrate. Different packing densities are simulated by varying the amount of lipids on the surface and allowing the monolayer to equilibrate. A water droplet is then placed on top of the lipid monolayer. When the packing density is high, no water molecules penetrate the monolayer and the contact angle is nearly 180° as shown in Figure 48. Since a contact angle this high is never seen in experiment, simulation of a nanometer sized water droplet at the molecular scale may not be a very accurate representation of the macro-scale contact angle experiments. Nonetheless, this approach can help us understand the relevant molecular force interactions.

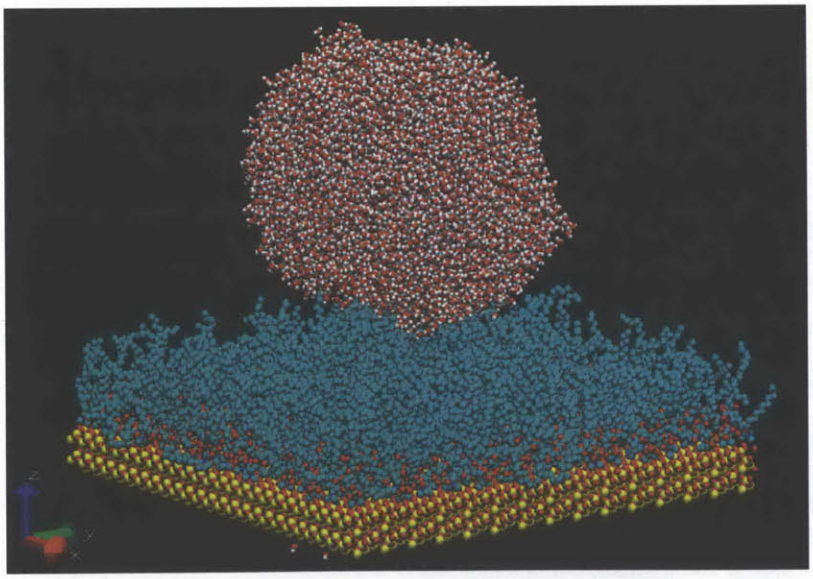

Figure 48: Water droplet on DPPC monolayer on quartz with a packing of 57 $Å^2$/molecule has a 180° contact angle.

When the packing density is lower, a small pinhole defect in the monolayer can cause water to "see" the underlying quartz and subsequently wet it. In doing so, the water becomes completely adsorbed onto the substrate while moving lipids aside as shown in Figure 49. This molecular rearrangement may be the mechanism of surface alteration that was observed for formamide and water.

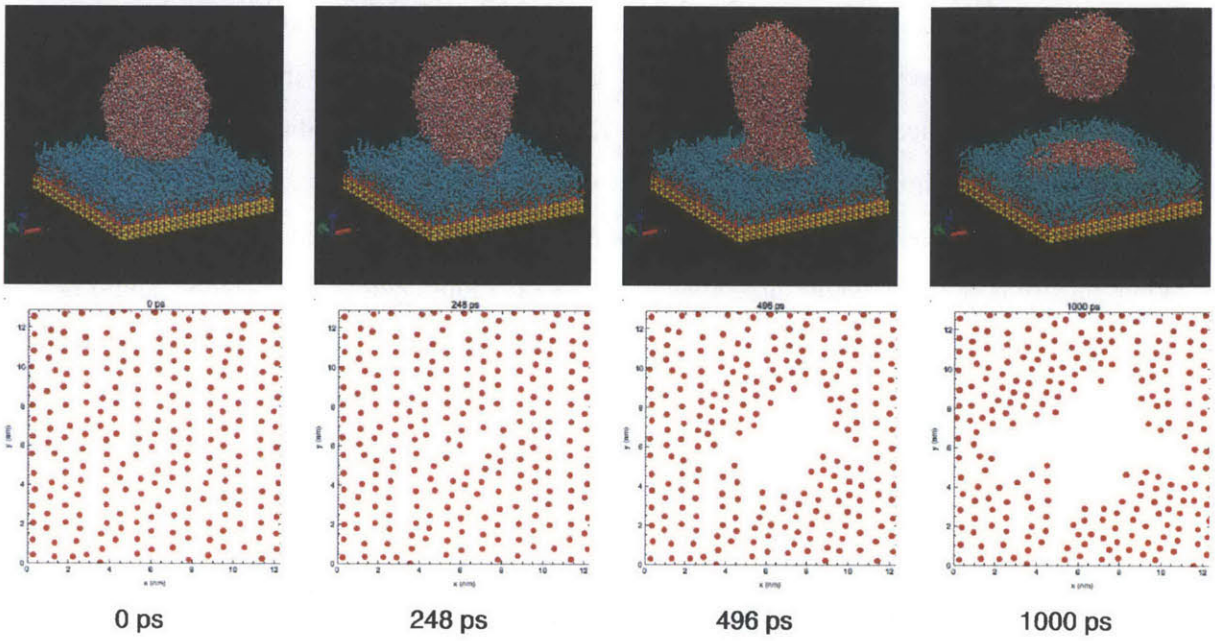

Figure 49: Progression of wetting of water drop on DPPC monolayer on quartz with a packing of 71 $Å^2$/molecule. The plots correspond to positions of lipid heads on the substrate and show a void forming in the center due to water displacement of the lipids.

According to the MD simulations, water has strong interactions with the quartz substrate such that tiny (~ 1 nm) defects can cause drastic changes in wettability. The surface can seem completely hydrophobic in the high density, defect free case but also completely wetting when defects arise. Once the underlying substrate becomes visible to the liquid, the wetting behavior is now dictated by hydrophobic and hydrophilic surface energies.

The results of the formamide and water experiments are consistent with what is known about mixed surface energy wetting [29]. During the advancing state, when the three phase contact line is at a point where the surface energy transitions from a low contact angle region (mica/glass) to a high contact angle region (lipid monolayer), pinning occurs until the high contact angle is satisfied. As the three phase contact line continues to advance over the high

contact angle region, the contact angle remains at this high contact angle value. As soon as the three phase contact line reaches another low contact angle region, the local contact angle diminishes to the low contact angle associated with it. However, this causes a local curvature, which lowers the pressure locally (according to the Young-Laplace equation) and causes an instability thereby advancing the three phase contact line very quickly across the low contact angle region until it reaches the next high contact angle region. This local curvature is due to the fact that the "apparent" macro-scale contact angle is high. Because the droplet quickly moves across the low contact angle region, more time is spent along the high contact angle region and hence the advancing contact angle measured is more associated with the high contact angle material. Therefore, the advancing contact angles were high for water and formamide due to the droplet wetting more of the lipid tails than mica/glass.

The opposite is the case in the receding state. When the three phase contact line transitions from the low contact angle region to the high contact angle region, the local contact angle instantly increases, causing a local high pressure to quickly traverse the high contact angle region. Since more time is spent along the low contact angle material, the receding angle is more associated with the low contact angle material. Therefore, water and formamide had low receding contact angles due to the droplet seeing more of the mica/glass than the lipid tails.

Surface Energy of Lipid Tails

Assuming that the higher contact angles of water and formamide on DPPC are representative of the true contact angle in the absence of defects, one can use the LWAB approach to determine the surface energy as described in Chapter 1. In order to do so, the following values of LWAB surface energies from literature [30] and measured static contact angles were used (Table 3).

Table 3: LWAB components of surface energies for water, formamide, and diiodomethane [30]

Probe liquid	γ (mN/m)	γ^{LW} (mN/m)	γ^{+} (mN/m)	γ^{-} (mN/m)	γ^{AB} (mN/m)	Contact Angle (°)
Water	72.8	21.8	25.5	25.5	51.0	97 ± 3
Formamide	58.0	39.0	2.28	39.6	19.0	88 ± 2
Diiodomethane	50.8	50.8	0	0	0	68 ± 2

Applying Equation 13 for each liquid yields the following LWAB surface energies for the lipid tails.

Table 4: LWAB surface energies for DPPC monolayer tail

γ (mN/m)	γ^{LW} (mN/m)	γ^{AB} (mN/m)
20.6 ± 2.8	24.0 ± 1.1	-3.4 ± 2.8

The result is that the tails have a total surface energy that is mostly dominated by Lifshitz-van der Waals interactions rather than electrostatic interactions. Lifshitz-van der Waals interaction dominate because the fatty acid tail is highly nonpolar and should be mostly dominated by nonpolar interactions.

Chapter 6: Closing

Summary

Lipid bilayers have remarkable permeability behavior under electric fields and this has many possible engineering applications, including high permeability water desalination membranes. The aqueous pore formation theory states that an electric potential lowers the energy barrier for pore expansion and that reversibility can be attained when this energy barrier is changed dynamically. This theory, which is largely dictated by surface and edge energies, is not a predictive theory that can allow us determine these surface and edge energies based on fundamental molecular interactions and chemical composition of the lipids. Before an ideal, highly tunable electroporation membrane can be formed, a through understanding of how the relevant parameters affect electroporation behavior must be gained.

In the beginning of this study, we sought to demonstrate the basic electroporation behavior and verify our electrical circuit model of electroporation. We have built a setup where fully hydrated DiPhyPC bilayers can be formed by the monolayer folding method. By applying a voltage ramp, we were able to verify the breakdown voltage where pores expand until rupture. An impedance spectroscopy setup was built and used to probe the electrical behavior of lipid bilayers. As expected, the lipid bilayer can be modeled as a parallel resistor-capacitor circuit. The bilayer also has a finite resistance, which indicates ions are somewhat permeable to the membrane possibly due to the existence of metastable pores.

To better understand the relevant molecular interactions and how electroporation relates to surface energies, we developed a model where the bilayer has separate head and tail contributions where the bulk of this study has been focused on determining the tail interaction. An experimental method to determine surface energies of these heads and tails is to perform sessile drop contact angle experiments on lipid bilayers and monolayers respectively. DPPC bilayers were formed via vesicle fusion. AFM was used to verify the existence of bilayers by measuring the height of bilayer patches and confirming that these heights correspond to twice the height of the lipid bilayer. The bilayers, however, were unstable in air and complete substrate coverage was unattainable unless the bilayer was kept submerged in fluid. In-fluid AFM was able to verify that near complete coverage was possible. Because of the instability in air, sessile

drop experiments were not performed for the lipid bilayer. DPPC monolayers were formed by Langmuir-Blodgett deposition on glass substrates. Using AFM again, the coverage by DPPC was verified and found to be fairly uniform except for certain defects due to vesicle adsorption. High hysteresis was observed for the sessile droplet experiments with water. From AFM, it was found that water altered the surface of the lipid coated substrate; thus, low receding angles are likely to be a result of the strong water-glass interaction.

In order to better characterize the wetting characteristics of the tails, a more suitable substrate, mica, was used along with three different probe liquids (water, formamide, and diiodomethane). Using mica, it was found the quality of DPPC coatings varied greatly with the surface pressure because of the crystallographic nature of DPPC. At sufficiently high surface pressures, the coverage was fairly uniform. When performing contact angle experiments, water and formamide both exhibited high contact angle hysteresis similar to that of the water-glass experiments because of the strong polar interaction that water and formamide have with mica. AFM revealed that both of these fluids alter the coated substrates. These results are in agreement with molecular dynamics simulations that show that a tiny defect can cause water to interact with the underlying substrate and change the wetting behavior dramatically. Diiodomethane on the other hand is nonpolar and did not exhibit a high hysteresis. In addition, AFM showed that diiodomethane did not alter the coated substrate. The high hysteresis of water and formamide is likely a result of having mixed surface energies where advancing contact angles are more associated with the lipid tails and the receding contact angles are more associated with the underlying substrate. Combining results from all three probe liquids, a total surface energy of the lipid tail was determined. It was found that the tail surface tension is highly dictated by nonpolar, van der Waals interactions as expected of a fatty acid chain.

Conclusions and Future Work

The results of this study have confirmed our understanding that lipid tail interactions are mostly nonpolar. How the magnitude of this interaction changes according to chemical compositional parameters of lipids must now be determined. One possible parameter is the packing density of the lipids since closer packed tails would have a stronger attractive interaction, thereby possibly increasing the overall surface tension. From our experiments, however, surface pressure does not affect the wetting behavior suggesting that either the effect of packing density is small or the packing density is not actually being altered. The latter case could

possibly be explained by the fragmenting of crack defects seen on mica at different surface pressures where the lipids may have an equilibrium packing density. To fully understand the packing behavior, the molecular packing density must be measured either by STM or by more precise AFM in the future.

Another possible parameter is the number of unsaturations in the lipid tail. Unsaturations are double bonds between adjacent carbons in the tail, which have the effect of producing a kink in the tail. Kinking reduces the overall effective packing density and thereby reduces the overall surface tension.

Surface energy can also be parameterized by the length of carbons in the lipid tail. The surface energy should linearly increase the average van der Waals interaction between lipids. In doing so, γ_{tail} can be modified independently of γ_{head}; thus, the relative importance of heads and tails to the total surface tension could be determined from experiments.

Modifying the cholesterol content is also likely to change the surface tension of the bilayer. Cholesterol has been known to regulate the fluidity of mammalian cell membranes. It is suggested that cholesterol promotes tighter packing due to its ring based structure [31]. Furthermore, previous experimental studies have shown that cholesterol enhances reversibility of electroporation. Hence, a link between cholesterol and surface energy is likely.

We have shown that bilayers are unstable in air; therefore, an alternative method to characterize the surface energy of the heads must be developed. One possible method involves performing contact angle experiments in water where the probe liquid would be a higher density liquid. The surface tension should also be comparable to water such that a measurable contact angle arises.

Once we gain an understanding of the relevant parameters affecting surface energy, electroporation experiments must be conducted where the effects of these parameters on the electroporation behavior can be directly observed. Electroporation experiments would also help us determine whether the aqueous pore formation theory as it stands now needs modification to fully describe the phenomenon. A better understanding of the phenomenon would, as stated before, help us to develop ideal highly tunable membranes for desalination, filtering and nano-gating applications.

Appendix

Ruby Code for Instrument Control

instruments.rb

This code is used as a back end to define all instrument control methods.

```
require 'rubygems'
require 'sicl'

# Syringe
pump*************************************************************************************
class Pump
  def initialize(aDiameter = 14.7, aRate = 8.0, aCOMPort = 3)
    @io = SICL.open("COM" + aCOMPort.to_s)
    @io.write("mmd " + aDiameter.to_s + "\r\n")
    @io.read
    @io.write("mlm " + aRate.to_s + "\r\n")
    @io.read
  end
  def close
    @io.close
  end
  def infuse
    @io.write("run\r\n")
    return @io.read.chomp
  end
  def withdraw
    @io.write("rev\r\n")
    return @io.read.chomp
  end
  def stop
    @io.write("stp\r\n")
    return @io.read.chomp
  end
  def diameter
    @io.write("dia\r\n")
    @io.read
    return @io.read.chomp.to_f
  end
  def rate(aRate = nil)
    if aRate == nil
      @io.write("rat\r\n")
      @io.read
      return @io.read.chomp.to_f
    else
      @io.write("mlm " + aRate.to_s + "\r\n")
      @io.read
      @io.write("rat\r\n")
      if @io.read.chomp == "OOR"
        @io.read
      end
      return @io.read.chomp.to_f
    end
  end
end

#
Oscilloscope*****************************************************************************************
*
class Scope

  def initialize
```

```
  @io = SICL.open("usb0[2391::5973::MY48260496::0]")
  acquire_normal
  trigger_source("external")
  @io.output(":tim:mode main")
  @io.output(":tim:ref left")
  stop
end

def close
  @io.close
end

def identity
  return @io.query("*IDN?")
end

def digitize
  initialSTB = @io.spoll
  initialESE = @io.query("*ESE?")
  @io.output("*ESE 1")
  @io.output(":dig chan1,chan2,chan3,chan4")
  @io.output("*OPC")
  while initialSTB == @io.spoll
    sleep 0.1
  end
  @io.query("*ESR?")
  @io.output("*ESE " + initialESE.to_s)
end

def run
  @io.output(":run")
end

def stop
  @io.output(":stop")
end

def waveforms

  #Define number of points
  number_of_points = 1000

  #Acquire waveforms and put into @waveforms
  @io.output(":wav:points " + number_of_points.to_s)
  @io.output(":wav:form byte")
  @waveforms = Array.new
  v_scales = voltage_scales
  v_offsets = voltage_offsets
  for j in 1..4
    @io.output(":wav:sour chan" + j.to_s)
    data = @io.query(":wav:data?")
    data = data[10..number_of_points + 9]
    waveform = Array.new
    for i in 0..data.length - 1 do
      waveform[i] = map_datum_to_voltage(data[i], v_scales[j - 1], v_offsets[j - 1])
    end
    @waveforms[j - 1] = waveform
  end

  #Build time array and prepend to @waveforms
  time_array = Array.new
  total_time = time_scale * 10
  for i in 0..number_of_points - 1 do
    time_array[i] = (i / (number_of_points.to_f - 1)) * total_time
  end
  @waveforms.unshift(time_array)

  return @waveforms
end

def save(aFilename = "default.csv")
  aFile = File.new(aFilename,"w+")
```

```
    for i in 0..@waveforms[0].length - 1 do
      for j in 0..@waveforms.length - 1 do
        aFile.syswrite(@waveforms[j][i].to_s + ",")
      end
      aFile.syswrite("\n")
    end
    aFile.close
  end

  def map_datum_to_voltage(aDatum, aVoltageScale, aVoltageOffset)
    voltage_per_unit = aVoltageScale / 31.875
    offset_in_units = aVoltageOffset / voltage_per_unit
    return (aDatum - (129 - offset_in_units)) * voltage_per_unit
  end

  def time_scale(*aTime)
    if aTime == []
      return @io.query(":tim:scale?").to_f
    else
      @io.output(":tim:scale " + aTime.to_s)
      return @io.query(":tim:scale?").to_f
    end
  end

  def voltage_scales
    @voltage_scales = Array.new
    for i in 1..4 do
      @io.output(":chan" + i.to_s + ":scale?")
      @voltage_scales[i - 1] = @io.enter.to_f
    end
    return @voltage_scales
  end

  def voltage_scale(aChannel, *aVoltage)
    if aVoltage == []
      return @io.query(":chan" + aChannel.to_s + ":scale?").to_f
    else
      @io.output(":chan" + aChannel.to_s + ":scale " + aVoltage.to_s)
      return @io.query(":chan" + aChannel.to_s + ":scale?").to_f
    end
  end

  def voltage_offsets
    @voltage_offsets = Array.new
    for i in 1..4 do
      @io.output(":chan" + i.to_s + ":offset?")
      @voltage_offsets[i - 1] = @io.enter.to_f
    end
    return @voltage_offsets
  end

  def voltage_offset(aChannel, *aVoltage)
    if aVoltage == []
      return @io.query(":chan" + aChannel.to_s + ":offset?").to_f
    else
      @io.output(":chan" + aChannel.to_s + ":offset " + aVoltage.to_s)
      return @io.query(":chan" + aChannel.to_s + ":offset?").to_f
    end
  end

  def coupling(aChannel, *aCoupling)
    if aCoupling == []
      return @io.query(":chan" + aChannel.to_s + ":coupling?").to_s
    else
      @io.output(":chan" + aChannel.to_s + ":coupling " + aCoupling.to_s)
      return @io.query(":chan" + aChannel.to_s + ":coupling?").to_s
    end
  end

  def trigger_coupling(*aCoupling)
    if aCoupling == []
      return @io.query(":trigger:edge:coupling?").to_s
```

```
    else
      @io.output(":trigger:edge:coupling " + aCoupling.to_s)
      return @io.query(":trigger:edge:coupling?").to_s
    end
  end

  def measure_vpp(aChannel)
    return @io.query(":measure:vpp? chan" + aChannel.to_s).to_f
  end

  def measure_average(aChannel)
    return @io.query(":measure:vaverage? chan" + aChannel.to_s).to_f
  end

  def acquire_averaging(aCount)
    @io.output("acquire:count " + aCount.to_i.to_s)
    @io.output(":acq:type average")
  end

  def acquire_normal
    @io.output(":acq:type norm")
  end

  def trigger_source(*aSource)
    if aSource == []
      return @io.query(":trigger:edge:source?").to_s
    else
      @io.output(":trigger:edge:source " + aSource.to_s)
      return @io.query(":trigger:edge:source?").to_s
    end
  end
end

# Function
generator*******************************************************************************
class Generator

  def initialize
    @io = SICL.open("usb0[1689::834::C021252::0]")
    output_impedance("inf")
    @io.output("trig:seq:sour ext")
  end

  def close
    @io.close
  end

  def identity
    @io.output("*IDN?")
    return @io.enter
  end

  def output_on
    @io.output("outp:stat on")
  end

  def output_off
    @io.output("outp:stat off")
  end

  def burst_on
    @io.output("sour1:burs:stat on")
  end

  def burst_off
    @io.output("sour1:burs:stat off")
  end

  def ramp_burst(aLow, aHigh, aPeriod)

    shape("ramp")
    burst_on
```

```
  @io.output("sour1:burs:ncyc 1")
  low(aLow)
  high(aHigh)
  phase("-180 deg")
  period(aPeriod)
  ramp_symmetry(100)
end

def square(aLow, aHigh, aDuration)
  shape("square")
  burst_off
  low(aLow.to_f)
  high(aHigh.to_f)
  period(aDuration.to_f * 2.0)
end

def ten_square(anOffset)
  shape("square")
  burst_off
  low(-0.025 + anOffset)
  high(0.025 + anOffset)
  frequency(5000)
end

def dc(aVoltage = 0)
  burst_off
  shape("dc")
  offset(aVoltage)
end

def ramp_symmetry(*aSymmetry)
  if aSymmetry == []
    return @io.query("sour1:func:ramp:symm?").to_f
  else
    @io.output("sour1:func:ramp:symm " + aSymmetry.to_s)
    return @io.query("sour1:func:ramp:symm?").to_f
  end
end

def output_impedance(*anImpedance)
  if anImpedance == []
    return @io.query("outp:imp?").to_f
  else
    @io.output("outp:imp " + anImpedance.to_s)
    return @io.query("outp:imp?").to_f
  end
end

def shape(*aShape)
  if aShape == []
    return @io.query("sour1:func:shap?")
  else
    @io.output("sour1:func:shap " + aShape.to_s)
    return @io.query("sour1:func:shap?")
  end
end

def offset(*anOffset)
  if anOffset == []
    return @io.query("sour1:volt:lev:imm:offs?").to_f
  else
    @io.output("sour1:volt:lev:imm:offs " + anOffset.to_s)
    return @io.query("sour1:volt:lev:imm:offs?").to_f
  end
end

def high(*aHigh)
  if aHigh == []
    return @io.query("sour1:volt:lev:imm:high?").to_f
  else
    @io.output("sour1:volt:lev:imm:high " + aHigh.to_s)
    return @io.query("sour1:volt:lev:imm:high?").to_f
```

```
    end
  end

  def low(*aLow)
    if aLow == []
      return @io.query("sour1:volt:lev:imm:low?").to_f
    else
      @io.output("sour1:volt:lev:imm:low " + aLow.to_s)
      return @io.query("sour1:volt:lev:imm:low?").to_f
    end
  end

  def frequency(*aFrequency)
    if aFrequency == []
      return @io.query("sour1:freq?").to_f
    else
      @io.output("sour1:freq " + aFrequency.to_s)
      return @io.query("sour1:freq?").to_f
    end
  end

  def period(*aPeriod)
    if aPeriod == []
      return 1 / @io.query("sour1:freq?").to_f
    else
      @io.output("sour1:freq " + (1 / aPeriod[0].to_f).to_s)
      return 1 / @io.query("sour1:freq?").to_f
    end
  end

  def phase(*aPhase)
    if aPhase == []
      return @io.query("sour1:phas:adj?").to_f
    else
      @io.output("sour1:phas:adj " + aPhase.to_s)
      return @io.query("sour1:phas:adj?").to_f
    end
  end

end

# Current
amplifier**********************************************************************************
class Amp

  def initialize
    @io = SICL.open("COM5")
    @io.output("++auto 0")
    @io.output("++addr 22")
    @gain = gain(3)
    correct
    zero_check_off
  end

  def close
    @io.close
  end

  def gain(*aGain)
    if aGain == []
      @io.output("U3X")
      return @gain = (@io.query("++read"))[2..3].to_i
    else
      @io.output("R" + aGain.to_s + "X")
      return @gain = aGain[0].to_i
    end
  end

  def correct
    @io.output("C2X")
    sleep 3
  end
```

```
  def zero_check_off
    @io.output("C0X")
  end

  def zero_check_on
    @io.output("C1X")
  end
end
```

instrument_control.rb

This code is used as a front end to control instruments and perform electroporation and impedance tests.

```
#!/usr/bin/env ruby

require "instruments.rb"

class Array
  def sum
    inject(0.0) { |result, el| result + el }
  end

  def mean
    sum / size
    end
end


def setup
  puts "Initializing..."

  puts "Current amplifier..."
  $a = Amp.new
  puts "Done!"
  puts "Function generator..."
  $g = Generator.new
  puts "Done!"
  puts "Syringe pump 1..."
  #$p1 = Pump.new(14.7,8.0,6)
  puts "Done!"
  puts "Syringe pump 2..."
  #$p2 = Pump.new(14.5,5.0,6)
  puts "Done!"
  puts "Oscilloscope..."
  $s = Scope.new
  puts "Done!"

  #$p1.stop
  #$p2.stop
  $g.output_off
  $s.acquire_normal
  $g.output_impedance("inf")
  $s.voltage_offset(2, $s.voltage_scale(2, 10.0 / 6.0) * 3.0)
  $s.voltage_offset(1, $s.voltage_scale(1, 0.002) * 0)
  $s.time_scale(0.001)
  dc_mode
  $s.run
  $a.zero_check_on
  $g.dc(0)
  $g.output_on

  # Find offset
  puts "Finding offset..."
  offsets = Array.new
  values = Array.new
```

```
  for i in -5..5 do
    $g.dc(i.to_f / 1000.0)
    $s.digitize
    values << $s.measure_average(1).abs
    offsets << i
  end
  $offset = offsets[values.index(values.min)].to_f / 1000.0
  puts "Offset = " + $offset.to_s
  $g.dc($offset)

  $s.voltage_offset(1, $s.voltage_scale(1, 1.0 / 6.0) * 3.0)

  puts "Ready!"
  monitor
end

def listen
  begin
    system("stty raw -echo")
    str = STDIN.getc
  ensure
    system("stty -raw echo")
  end
  if str.chr != "q"
    keystroke = case str.chr
      when "z" then withdraw_fast(1)
      when "x" then stop_pump(1)
      when "c" then infuse_fast(1)
      when "d" then infuse_slow(1)
      when "a" then withdraw_slow(1)
      when "v" then withdraw_fast(2)
      when "b" then stop_pump(2)
      when "n" then infuse_fast(2)
      when "h" then infuse_slow(2)
      when "f" then withdraw_slow(2)
      when "0" then monitor(0.0)
      when "1" then monitor(0.001)
      when "2" then monitor(0.01)
      when "3" then monitor(0.1)
      when "4" then monitor(0.5)
      when "5" then monitor(1.0)
      when "=" then increase_gain
      when "-" then decrease_gain
      when " " then measure
      when "s" then square
      else puts "Unknown command " + str.to_s
    end
  listen
  end
end

def monitor(aVoltage = 0)
  $a.zero_check_on
  if aVoltage == 0
    $s.voltage_offset(1, $s.voltage_scale(1, 1.0 / 6.0) * 3.0)
  else
    $s.voltage_offset(1, $s.voltage_scale(1, aVoltage / 6.0) * 3.0)
  end
  $g.dc(aVoltage + $offset)
  $s.time_scale(0.001)
  $s.voltage_offset(2, $s.voltage_scale(2) * 3.0)
  dc_mode
  $s.run
  $a.zero_check_off
end

def withdraw_fast(aPump)
  if aPump ==  1
    p = $p1
  else
    p = $p2
  end
```

```
  p.rate(5.0)
  p.withdraw
  puts "Pump withdrawing..."
end

def withdraw_slow(aPump)
  if aPump ==  1
    p = $p1
  else
    p = $p2
  end
  p.rate(0.5)
  p.withdraw
  puts "Pump withdrawing..."
end

def stop_pump(aPump)
  if aPump ==  1
    p = $p1
  else
    p = $p2
  end
  p.stop
  puts "Pump stopped"
end

def infuse_fast(aPump)
  if aPump ==  1
    p = $p1
  else
    p = $p2
  end
  p.rate(5.0)
  p.infuse
  puts "Pump infusing..."
end

def infuse_slow(aPump)
  if aPump ==  1
    p = $p1
  else
    p = $p2
  end
  p.rate(0.5)
  p.infuse
  puts "Pump infusing..."
end

def reset_gain
  $a.gain(3)
  $s.voltage_offset(2, $s.voltage_scale(2, 10.0 / 6.0) * 3.0)
  puts "Gain reset"
end

def increase_gain
  $a.gain($a.gain + 1)
  puts "Gain set to " + $a.gain.to_s
end

def decrease_gain
  $a.gain($a.gain - 1)
  puts "Gain set to " + $a.gain.to_s
end

def find_best_gain
  $s.stop
  $a.gain(3)
  $s.voltage_offset(2, $s.voltage_scale(2, 10.0 / 6.0) * 3.0)
  puts "Finding best gain..."
  $s.digitize

  while $s.measure_average(2).to_f < 0.9
```

```
    $a.gain($a.gain.to_i + 1)
    sleep 0.5
    $s.digitize
  end
  puts "Adjusting voltage scales..."
  $s.digitize
  $s.voltage_offset(2, $s.voltage_scale(2, $s.measure_average(2).to_f / 6.0) * 3.0)
  $s.run
  puts "Done!"
end

def measure
  print "Which test?\n1. Impedance\n2. Breakdown\n3. Digitize and save current waveform\n"
  response = gets.to_s.chomp
  if response == "1"
    impedance_test
  elsif response == "2"
    breakdown_test
  elsif response == "3"
    digitize_save
  end
end

def impedance_test
  # Prompt user for filename prefix (default = "default_impedance_")
  print "Filename prefix? "
  filename = gets.to_s.chomp
  if filename == ""
    filename = "default_impedance_"
  end

  # Prompt user for peak-to-peak voltage (default = 50 mV)
  print "Peak to peak voltage (mV)? "
  vpp = gets.to_s.chomp
  if vpp == ""
    vpp = 0.05
  else
    vpp = vpp.to_f / 1000.0
  end

  # Prompt user for low frequency (default = 0.1 Hz)
  print "Low frequency (Hz)? "
  lf = gets.to_s.chomp
  if lf == ""
    lf = 0.1
  else
    lf = lf.to_f
  end

  # Prompt user for high frequency (default = 100,000 Hz)
  print "High frequency (Hz)? "
  hf = gets.to_s.chomp
  if hf == ""
    hf = 100000.to_f
  else
    hf = hf.to_f
  end

  # Prompt user for number of steps (default = 20 steps)
  print "Number of steps? "
  num_steps = gets.to_s.chomp
  if num_steps == ""
    num_steps = 20
  else
    num_steps = num_steps.to_i
  end

  # Prompt user to choose linear or logarithmic (default = logarthmic)
  print "Linear (0) or Logarthmic (1)? "
  linlog = gets.to_s.chomp
  if linlog == ""
    linlog = 1
```

```
else
  linlog = linlog.to_i
end

# Setup frequency array
freqs = Array.new
if linlog == 1
  step_size = (Math.log(hf) - Math.log(lf)) / (num_steps - 1)
  for i in 0..(num_steps - 1) do
    freqs[i] = Math.exp(Math.log(lf) + i*step_size)
  end
else
  step_size = (hf - lf) / (num_steps - 1)
  for i in 0..(num_steps - 1) do
    freqs[i] = lf + i*step_size
  end
end

#Start testing
$s.stop
dc_mode
gains = Array.new

#Test frequencies
puts "Testing frequencies"
for n in 0..(num_steps - 1) do
  puts "Frequency: " + freqs[n].to_s
  $s.voltage_offset(1, $s.voltage_scale(1, vpp / 6.0) * 0.0)
  $s.voltage_offset(2, $s.voltage_scale(2, 0.2 / 6.0) * 0.0)
  $s.time_scale(1.0 / (5.0 * 2.0 * freqs[n]))
  $s.voltage_offset(2, 0)
  $g.shape("sin")
  $g.burst_off
  $g.low(-vpp / 2 + $offset)
  $g.high(vpp / 2 + $offset)
  $g.frequency(freqs[n])
  $s.trigger_source("external")
  $a.gain(3)
  puts "Gain: " + $a.gain().to_s
  $s.digitize
  $s.digitize
  cpp = 0

  while (cpp = $s.measure_vpp(2)) < 0.15 && $a.gain < 10
    $s.voltage_offset(2, 0*$s.measure_average(2))
    $a.gain($a.gain.to_i + 1)
    puts "Gain: " + $a.gain().to_s
    $s.acquire_averaging(128)
    $s.digitize
  end
  gains << $a.gain()
  $s.voltage_scale(2, 5.0 / 6.0)
  $s.voltage_offset(2, 0*$s.measure_average(2))
  $s.time_scale(1.0 / (2*2.0 * freqs[n]))
  $s.acquire_averaging(256)
  $s.digitize
  sleep 1
  cpp = $s.measure_vpp(2)

  $s.voltage_scale(2, cpp / 6.0)
  $s.voltage_offset(2, 0*$s.measure_average(2))
  $s.time_scale(1.0 / (2.0 * freqs[n]))



  $s.acquire_averaging([512*$s.time_scale*10,5].max/($s.time_scale*10))
  $s.digitize
  sleep 1
  waveforms = $s.waveforms
  $s.acquire_normal
  currentArray = waveforms[2]
  newCurrentArray = Array.new
```

```
    aGain = $a.gain
    for i in 0..currentArray.length - 1 do
      newCurrentArray[i] = currentArray[i] / 10.0 ** aGain
    end
    waveforms[2] = newCurrentArray

    aFile = File.new(filename + n.to_s + ".csv","w+")
    for i in 0..waveforms[0].length - 1 do
      for j in 0..waveforms.length - 1 do
        aFile.syswrite(waveforms[j][i].to_s + ",")
      end
      aFile.syswrite("\n")
    end
    aFile.close
  end

  #Write gains file
  aFile = File.new(filename + "gains.csv","w+")
  for i in 0..gains.length - 1 do
    aFile.syswrite((10.0**gains[i].to_f).to_s + ",")
    aFile.syswrite("\n")
  end
  aFile.close

  #Write freqs file
  aFile = File.new(filename + "freqs.csv","w+")
  for i in 0..freqs.length - 1 do
    aFile.syswrite(freqs[i].to_s + ",")
    aFile.syswrite("\n")
  end
  aFile.close

  puts "Finished impedance test"
end

def breakdown_test
  # Prompt user for filename (default = "default_breakdown.csv")
  print "Filename? "
  filename = gets.to_s.chomp
  if filename == ""
    filename = "default_breakdown.csv"
  else
    filename = filename + ".csv"
  end

  # Prompt user for end voltage (default = 1 V)
  print "End voltage (mV)? "
  endVoltage = gets.to_s.chomp
  if endVoltage == ""
    endVoltage = 1.0
  else
    endVoltage = endVoltage.to_f / 1000.0
  end

  # Promp user for ramp time (default = 100 us)
  print "Ramp time (us)? "
  rampTime = gets.to_s.chomp
  if rampTime == ""
    rampTime = 0.0001
  else
    rampTime = rampTime.to_f / 1000000.0
  end

  # Start!
  $s.stop
  dc_mode
  $s.voltage_offset(2, $s.voltage_scale(2) * 3.0)
  $g.ramp_burst($offset, endVoltage + $offset, rampTime)
  $s.voltage_offset(1, $s.voltage_scale(1, endVoltage / 6.0) * 3.0)
  $s.time_scale(rampTime / 8.0)
  puts "Digitizing..."
  $s.digitize
```

```
  waveforms = $s.waveforms
  currentArray = waveforms[2]
  newCurrentArray = Array.new
  aGain = $a.gain
  for i in 0..currentArray.length - 1 do
    newCurrentArray[i] = currentArray[i] / 10.0 ** aGain
  end
  waveforms[2] = newCurrentArray

  $g.dc($offset)

  # Save
  puts "Saving..."
  aFile = File.new(filename,"w+")
  for i in 0..waveforms[0].length - 1 do
    for j in 0..waveforms.length - 1 do
      aFile.syswrite(waveforms[j][i].to_s + ",")
    end
    aFile.syswrite("\n")
  end
  aFile.close
  puts "Breakdown test finished!"
end

def digitize_save
  # Prompt user for filename (default = "default_waveform.csv")
  print "Filename? "
  filename = gets.to_s.chomp
  if filename == ""
    filename = "default_waveform.csv"
  else
    filename = filename + ".csv"
  end

  $s.digitize
  waveforms = $s.waveforms
  currentArray = waveforms[2]
  newCurrentArray = Array.new
  aGain = $a.gain
  for i in 0..currentArray.length - 1 do
    newCurrentArray[i] = currentArray[i] / 10.0 ** aGain
  end
  waveforms[2] = newCurrentArray

  # Save
  puts "Saving..."
  aFile = File.new(filename,"w+")
  for i in 0..waveforms[0].length - 1 do
    for j in 0..waveforms.length - 1 do
      aFile.syswrite(waveforms[j][i].to_s + ",")
    end
    aFile.syswrite("\n")
  end
  aFile.close
  puts "Waveform saved!"
end

def square
  $g.ten_square($offset)
  $s.voltage_offset(1, $s.voltage_scale(1, 0.04 / 6.0) * 0.0)
  $s.time_scale(0.0001)
  $s.voltage_offset(2, 0)
  dc_mode
  $s.run
  puts "square wave"
end

def ac_mode
  $s.coupling(1, "ac")
  $s.coupling(2, "ac")
  $s.trigger_coupling("lfr")
end
```

```
def dc_mode
  $s.coupling(1, "dc")
  $s.coupling(2, "dc")
  $s.trigger_coupling("dc")
end

def quit
  $s.stop
  #$p1.stop
  #$p2.stop
  $g.output_off
  $a.gain(3)
  $a.zero_check_on

  $a.close
  $g.close
  #$p1.close
  #$p2.close
  $s.close

  puts "Quit"
end


#Steps
setup

listen

quit
```

References

[1] G. Sersa, M. Cemazar, and M. Snoj, "Electrochemotherapy of tumours," *Current Oncology*, vol. 16, no. 2, p. 34, 2009.

[2] O. P. B. O. Publishing, *World Energy Outlook 2005: Middle East and North Africa Insights*. International Energy Agency, 2005.

[3] Y. Kaufman and A. Berman, "Supported lipid bilayer membranes for water purification by reverse osmosis," *Langmuir*, 2010.

[4] M. Malmsten, "Protein Adsorption at Phospholipid Surfaces," *Journal of Colloid and Interface Science*, vol. 172, no. 1, pp. 106-115, Jun. 1995.

[5] K. Kull, M. Steen, and E. Fisher, "Surface modification with nitrogen-containing plasmas to produce hydrophilic, low-fouling membranes," *Journal of membrane science*, vol. 246, no. 2, pp. 203-215, 2005.

[6] A. Reddy et al., "Fouling resistant membranes in desalination and water recovery," *Desalination*, vol. 183, no. 1, pp. 301-306, 2005.

[7] A. Kikuchi, "Pulsatile drug release control using hydrogels," *Advanced drug delivery reviews*, 2002.

[8] H. Lindsey, N. O. Petersen, and S. I. Chan, "Physicochemical Characterization of 1,2-Diphytanoyl-Sn-Glycero-3-Phosphocholine in Model Membrane Systems," *Biochimica et Biophysica Acta (BBA)-Biomembranes*, vol. 555, no. 1, pp. 147-167, Jul. 1979.

[9] J. Crowley, "Electrical breakdown of bimolecular lipid membranes as an electromechanical instability," *Biophysical Journal*, 1973.

[10] U. Zimmermann, G. Pilwat, F. Beckers, and F. Riemann, "Effects of external electrical fields on cell membranes," *Bioelectrochemistry and Bioenergetics*, vol. 3, no. 1, pp. 58-83, 1976.

[11] M. Pavlin, T. Kotnik, D. Miklavcic, P. Kramar, and A. Macek Lebar, "Chapter Seven Electroporation of Planar Lipid Bilayers and Membranes," *Advances in Planar Lipid Bilayers and Liposomes*, vol. 6, pp. 165-226, 2008.

[12] R. Glaser, S. Leikin, L. Chernomordik, V. Pastushenko, and A. Sokirko, "Reversible electrical breakdown of lipid bilayers: formation and evolution of pores," *Biochimica et Biophysica Acta (BBA)-Biomembranes*, vol. 940, no. 2, pp. 275-287, 1988.

[13] L. Chernomordik et al., "The electrical breakdown of cell and lipid membranes: the similarity of phenomenologies," *Biochimica et Biophysica Acta (BBA)-Biomembranes*, vol. 902, no. 3, pp. 360-373, 1987.

[14] C. Chen, S. Smye, M. Robinson, and J. Evans, "Membrane electroporation theories: a review," *Medical and Biological Engineering and Computing*, vol. 44, no. 1, pp. 5-14, 2006.

[15] J. Teissie, M. Golzio, and M. Rols, "Mechanisms of cell membrane electropermeabilization: A minireview of our present (lack of ?) knowledge," *Biochimica Et Biophysica Acta-General Subjects*, vol. 1724, no. 3, pp. 270-280, 2005.

[16] S. Ho and G. Mittal, "Electroporation of cell membranes: a review," *Critical reviews in biotechnology*, vol. 16, no. 4, pp. 349-362, 1996.

[17] J. Weaver, "Electroporation theory," *Methods in Molecular Biology*, 1995.

[18] C. Van Oss, M. Chaudhury, and R. Good, "Interfacial Lifshitz-van der Waals and polar interactions in macroscopic systems," *Chemical Reviews*, vol. 88, no. 6, pp. 927-941,

1988.
[19] C. J. van Oss, "Acid--base interfacial interactions in aqueous media," *Colloids and Surfaces A: Physicochemical and Engineering Aspects*, vol. 78, pp. 1-49, Oct. 1993.
[20] P. Mueller, D. Rudin, and H. T. Tien, "Reconstitution of cell membrane structure in vitro and its transformation into an excitable system," *Nature*, 1962.
[21] B. A. Suarez-Isla, K. Wan, J. Lindstrom, and M. Montal, "Single-channel recordings from purified acetylcholine receptors reconstituted in bilayers formed at the tip of patch pipets," *Biochemistry*, vol. 22, no. 10, pp. 2319-2323, May. 1983.
[22] A. Hirano-Iwata, M. Niwano, and M. Sugawara, "The design of molecular sensing interfaces with lipid-bilayer assemblies," *Trends in Analytical Chemistry*, 2008.
[23] M. Montal and P. Mueller, "Formation of bimolecular membranes from lipid monolayers and a study of their electrical properties," *Proceedings of the National Academy of Sciences*, vol. 69, no. 12, pp. 3561-3566, 1972.
[24] M. Colombini, "Characterization of channels isolated from plant mitochondria.," *Methods In Enzymology*, vol. 148, p. 465, 1987.
[25] P. Kramar, D. Miklavcic, and A. Lebar, "A System for the Determination of Planar Lipid Bilayer Breakdown Voltage and Its Applications," vol. 8, no. 2, 2009.
[26] R. Benz, F. Beckers, and U. Zimmermann, "Reversible electrical breakdown of lipid bilayer membranes: a charge-pulse relaxation study," *Journal of Membrane Biology*, vol. 48, no. 2, pp. 181-204, 1979.
[27] E. Castellana and P. Cremer, "Solid supported lipid bilayers: From biophysical studies to sensor design," *Surface Science Reports*, vol. 61, no. 10, pp. 429-444, 2006.
[28] B. Cross, A. Steinberger, and C. Cottin-Bizonne, "Boundary flow of water on supported phospholipid films," *EPL (Europhysics ...*, 2006.
[29] Van P Carey, *Liquid Vapor Phase Change Phenomena: An Introduction to the Thermophysics of Vaporization and Condensation Processes in Heat Transfer Equipment, Second Edition*, 2nd ed. Taylor & Francis, 2007, p. 600.
[30] Z. Li, R. F. Giese, W. Wu, M. F. Sheridan, and C. J. van Oss, "The Surface Thermodynamic Properties of Some Volcanic Ash Colloids," *Journal of Dispersion Science and Technology*, vol. 18, no. 3, pp. 223-241, 1997.
[31] W. Hung, M. Lee, F. Chen, and H. Huang, "The condensing effect of cholesterol in lipid bilayers," *Biophysical Journal*, vol. 92, no. 11, pp. 3960-3967, 2007.